The Astrophysical Journal, 812:11 (18pp), 2015 October 10 doi:10.1088/0004-637X/812/1/11

ELLERMAN BOMBS AT HIGH RESOLUTION. III. SIMULTANEOUS OBSERVATIONS WITH *IRIS* AND SST

G. J. M. Vissers[1], L. H. M. Rouppe van der Voort[1], R. J. Rutten[1,2], M. Carlsson[1], and B. De Pontieu[1,3]
[1] Institute of Theoretical Astrophysics, University of Oslo, P.O. Box 1029 Blindern, NO-0315 Oslo, Norway; g.j.m.vissers@astro.uio.no
[2] Lingezicht Astrophysics, 't Oosteneind 9, 4158CA Deil, The Netherlands
[3] Lockheed Martin Solar and Astrophysics Laboratory, 3251 Hanover Street, Org. A021S, Bldg. 252, Palo Alto, CA 94304, USA
Received 2015 February 1; accepted 2015 June 22; published 2015 October 5

ABSTRACT

Ellerman bombs (EBs) are transient brightenings of the extended wings of the solar Balmer lines in emerging active regions. We describe their properties in the ultraviolet lines sampled by the *Interface Region Imaging Spectrograph* (*IRIS*), using simultaneous imaging spectroscopy in Hα with the Swedish 1-m Solar Telescope (SST) and ultraviolet images from the Solar Dynamics Observatory for Ellerman bomb detection and identification. We select multiple co-observed EBs for detailed analysis. The *IRIS* spectra strengthen the view that EBs mark reconnection between bipolar kilogauss fluxtubes with the reconnection and the resulting bi-directional jet located within the solar photosphere and shielded by overlying chromospheric fibrils in the cores of strong lines. The spectra suggest that the reconnecting photospheric gas underneath is heated sufficiently to momentarily reach stages of ionization normally assigned to the transition region and the corona. We also analyze similar outburst phenomena that we classify as small flaring arch filaments and ascribe to reconnection at a higher location. They have different morphologies and produce hot arches in million-Kelvin diagnostics.

Key words: Sun: activity – Sun: atmosphere – Sun: magnetic fields

Supporting material: animations

1. INTRODUCTION

Ellerman (1917) discovered intense short-lived brightenings of the extended wings of the Balmer Hα line at 6563 Å that he called "solar hydrogen bombs." They have been called Ellerman bombs (henceforth EBs) since McMath et al. (1960). For more detail, we refer to the excellent summary by Georgoulis et al. (2002) and our more recent review of the extensive EB literature in Rutten et al. (2013).

We discuss the subsequent EBs literature below, but here point out the recent discovery by Peter et al. (2014) of very hot "bombs" in ultraviolet spectra from the *Interface Region Imaging Spectrograph* (*IRIS;* De Pontieu et al. 2014). The present paper addresses their suggestion that these bombs might have been EBs or similar to EBs.

A major motivation to study EBs is that they supposedly mark the locations of serpentine flux rope emergence in newly emerging active regions (e.g., Bernasconi et al. 2002; Pariat et al. 2004, 2009; Isobe et al. 2007; Archontis & Hood 2009). Understanding their nature may therefore present a way of measuring active region evolution, in particular the reconnective field topography evolution that eventually produces much larger solar outbursts. In this context, EBs should become useful as indicators of strong-field reconnection when well understood.

In addition, the complex physics and spectrum formation of the EB phenomenon are of interest per sé since EBs appear to be pockets of hot gas within the photosphere. The discovery of extremely hot *IRIS* bombs by Peter et al. (2014) that also appear to be photospheric enhances this interest. In our present series of EB analyses, we employ high-quality imaging spectroscopy with the Swedish 1-m Solar Telescope (SST; Scharmer et al. 2003) to study EBs at unprecedented spatial, spectral, and temporal resolution. Paper I (Watanabe et al. 2011) established that EBs are a purely photospheric phenomenon.

Paper II (Vissers et al. 2013) added evidence that EBs mark the magnetic reconnection of strong opposite-polarity field concentrations in the low photosphere and discussed their appearance in 1700 Å images from the Atmospheric Imaging Assembly (AIA; Lemen et al. 2012) of the *Solar Dynamics Observatory* (*SDO*).

Let us morphologically define the three bomb-like phenomena which we discuss below, based on our inspections of dozens of such features in the SST, *SDO*, and *IRIS* data. More detail on their recognition is given in Section 2.

We define EBs as substantial brightenings of the extended wings of Hα without core brightening which, at sufficient angular and temporal resolution, show definite rapid-flame morphology when viewed from aside, as described in Paper I. EB Hα wing brightenings exceed those from much more ubiquitous magnetic concentrations that also happen to appear bright in the Hα wings ("pseudo-EBs"; Rutten et al. 2013).

Next, we define "flaring arch filaments" (henceforth FAFs) as sudden fierce brightenings in AIA 1600 Å image sequences that differ from the EB brightenings also seen in this AIA channel by appearing with shorter duration and more abrupt changes, having elongated morphology, and showing fast apparent brightness motion along filamentary strands. Because they are usually much less evident in AIA 1700 Å images, their 1600 Å appearance is likely due to the brightening of the C IV doublet at 1548 and 1550 Å in AIA's 1600 Å passband. Their filamentary morphology and rapid evolution suggest that these are heating events, likely reconnection, that take place along the fibrilar canopy seen, for example, at the Hα line center, or eject heated matter along chromospheric field lines.

Finally, following Peter et al. (2014), we define "*IRIS* bombs" (henceforth IBs) as ultraviolet brightenings with substantial emission in the Si IV lines observed by *IRIS*, that show these with very wide and complex non-Gaussian profiles on which deep absorption blends of lower metal ionization stages are superimposed.

The visibility of EBs in AIA's 1700 Å images and the full-time, full-disk availability of the *SDO* data enables one to check any new observational EB study to determine whether or not it instead addresses pseudo-EBs or FAFs. We did so for the EB literature following the publication of Paper I and briefly comment on our scrutiny here.

We judge that the 3570 EBs of Nelson et al. (2013a) were probably pseudo-EBs, and likewise the 4 EBs of Nelson et al. (2013b). Both studies targeted decaying sunspots rather than emerging active regions.

In contrast, we recognized the 3 EBs of Bello González et al. (2013) as well-defined EBs in 1700 Å, indeed occurring in a complex region with much flux emergence. The same holds for at least EB3 and EB4 of Hong et al. (2014) and the single EB of Yang et al. (2013; which occurred a day after those of Bello González et al. 2013 in the same region). Most recently, the near-limb EBs in Nelson et al. (2015) have obvious flame morphology.

Generally, the latter papers confirm our view in Paper I, Paper II, and Rutten et al. (2013). EBs are strong-field opposite-polarity cancelations that occur in complex emerging active regions. They mark reconnection taking place in the photosphere, and produce substantial local heating that leaves no direct signature in the overlying chromosphere and transition region.

Modeling of the Hα-wing enhancements that characterize EBs was recently reported by Nelson et al. (2013b), Bello González et al. (2013), Hong et al. (2014), and Berlicki & Heinzel (2014). We return to these analyses in Section 4, but point out here that they agree with all earlier modeling in claiming upper-photosphere temperature enhancements of only 1000–5000 K, in obvious conflict with the notion that EBs might be IBs, for which Peter et al. (2014) suggest formation temperatures near 100,000 K.

Were the IBs of Peter et al. (2014) indeed EBs, as the authors suggested? Our similar inspection of the concurrent AIA 1700 and 1600 Å morphology was inconclusive. Their bomb B-1, with deep Ni II and Fe II absorption blends in the Si IV lines, seemed to be a bona fide EB, but the others looked more like FAFs. Hence, as stressed by Peter et al. (2014), there is a clear need for simultaneous *IRIS* and ground-based Hα observations of EBs and IBs because EB recognition is easier in Hα.

In this paper, we address this EB–IB issue by combining new EB and FAF observations with the SST with simultaneous observations with *IRIS* and *SDO*/AIA. Our conclusion is that both EBs and FAFs produce ultraviolet line profiles of IB type, and that these provide valuable insights and constraints.

Our observations are presented in the next section, and the results in Section 3. We present a discussion in Section 4 and conclude in Section 5.

2. OBSERVATIONS, REDUCTION, AND METHODS

2.1. Data Collection

For this study we analyzed data from multiple observing campaigns targeting emerging active regions with co-pointing of the SST and *IRIS*. The SST's CRisp Imaging Spectro-Polarimeter (CRISP; Scharmer et al. 2008), a Fabry–Pérot interferometer, collected imaging spectroscopy in at least Hα (further specification in Table 1).

The *IRIS* spectrograph (SG) recorded its standard selection of ultraviolet lines: the C II doublet near 1335 Å, the Si IV doublet at 1394 Å and 1403 Å, the Mg II h & k lines near 2796 Å and 2804 Å, including the overlapping wing part between them with various blends, in particular the Mg II triplet lines near 2798 Å (which are two overlapping transitions that overlap so closely that they look like one line in the spectrum). For more details, including characteristic formation temperatures, see Table 4 of De Pontieu et al. (2014). For *IRIS*-related formation studies of Mg II h & k, see Leenaarts et al. (2013a, 2013b) and Pereira et al. (2013); see Pereira et al. (2015) for a similar formation study of the Mg II triplet lines. In addition, *IRIS* collected slitjaw images (SJI) in the 1330, 1400, 2796, and 2832 Å channels, as detailed in Table 3 of De Pontieu et al. (2014).

In Table 1 we specify pointing, spectral, and timing details for the three particular data sets from these co-ordinated observing campaigns that were selected for this paper.

The top row of Figure 1 shows image samples of the first. It covered the major sunspot in active region AR 11836 that had a pronounced moat flow. *IRIS* supported these observations in a "four-step sparse raster" mode of slit motion, covering 3 arcsec with 2 s exposure times per step. This pattern gives good temporal resolution for a given spot on the Sun but smaller chance of hitting a scarce feature such as an EB.

Sample images for data sets 2 and 3 covering AR 12089 are similarly shown in the lower rows of Figure 1. For both data sets, *IRIS* took a dense synoptic raster of 96 steps, covering 31.35 arcsec at 4 s exposure time per step. The larger pattern width means that there is a larger spatial chance of hitting an EB, but the consequently low repeat cadence, longer than the typical EB appearance, diminishes the catch.

We also collected corresponding image sequences from *SDO*/AIA and *SDO*/HMI (Scherrer et al. 2012) using the JSOC image cutout service at Stanford University.

2.2. Data Reduction

The SST/CRISP data were reduced using the CRISPRED pipeline (de la Cruz Rodríguez et al. 2015). It includes (1) dark and flat field correction, (2) multi-object, multi-frame blind deconvolution (van Noort et al. 2005) to reduce the effects of high-order atmospheric seeing, (3) minimization of remaining small-scale deformation through cross-correlation (Henriques 2012), (4) prefilter transmission correction (de la Cruz Rodriguéz 2010), (5) correction for time-dependent image rotation due to the alt-azimuth telescope configuration, and (6) removal of remaining rubber sheet distortions by destretching (Shine et al. 1994).

The SST and *IRIS* data were co-aligned using far-wing images in Hα (dataset 1) or Ca II 8542 Å (data sets 2 and 3) and the *IRIS* Mg II h 2832 Å slitjaws. *SDO*/AIA 1600 Å or 1700 Å images (depending on the dataset) were used as initial co-location reference to define common features in the fields of view and their offsets. The SST data were then resampled to the *IRIS* slitjaw pixel size of 0.167 arcsec^2. Finally, sub-images (usually containing one or more pores) were then selected manually for cross-correlation at each time step.

The AIA and HMI image sequences were also precisely co-aligned with the full-resolution SST image sequences.

In the alignment and the data analysis we made much use of the CRisp SPectral EXplorer (CRISPEX; Vissers & Rouppe van der Voort 2012) for data browsing. The latest version (available through SolarSoft) can handle both FITS-formatted

Table 1
Overview of the Data Sets Analyzed in this Study

Set	Date	Target			Instrument	OBSID	Diagnostic Details					Time (UTC)
		AR	(X, Y) (″)	θ (°)			Name	λ_0 (Å)	Range[a] (Å)	$\Delta\lambda$ (mÅ)	Δt (s)	
1	2013 Sep 6	11836	(763, 129)	50.6	CRISP	⋯	Hα	6563	±1.2	100	5.5	08:15–09:01
					IRIS	4003004168	SG (4 × 1″)	⋯	⋯	⋯	11	08:11–11:39
							SJI 1330	1340	55	⋯	12	
							SJI 1400	1390	55	⋯	12	
							SJI 2796	2796	4	⋯	12	
							SJI 2832	2830	4	⋯	69	
2	2014 Jun 14	12089	(221, 278)	21.5	CRISP	⋯	Hα	6563	±1.4	200	11.4	07:20–08:11
						⋯	Ca II	8542	±1.2	100		
						⋯	Fe I	6302	−0.048[b]	⋯		
					IRIS	3820256197	SG (96 × 0.″33)	⋯	⋯	⋯	516	07:29–10:47
							SJI 1330	1340	55	⋯	17	
							SJI 1400	1390	55	⋯	17	
							SJI 2796	2796	4	⋯	17	
							SJI 2832	2830	4	⋯	86	
3	2014 Jun 15	12089	(411, 281)	31.0	CRISP	⋯	Hα	6563	±1.4	200	11.4	07:47–08:49
						⋯	Ca II	8542	±1.2	100		
						⋯	Fe I	6302	−0.048[b]	⋯		
					IRIS	3820256197	SG (96 × 0.″33)	⋯	⋯	⋯	516	07:29–10:55
							SJI 1330	1340	55	⋯	17	
							SJI 1400	1390	55	⋯	17	
							SJI 2796	2796	4	⋯	17	
							SJI 2832	2830	4	⋯	86	

Notes.
[a] This column gives the passband width in the case of the slitjaw image channels.
[b] Full Stokes polarization measurements were obtained at this wavelength position.

IRIS data including SJI, and legacy "La Palma"-format data files from the SST.

2.3. EB Identification Using Hα

Identifying EBs is not a trivial matter. A substantial part of the EB literature did not address actual EBs but "pseudo-EBs": magnetic concentrations (MC) in network or plage that likewise brighten in the Hα wings, as explained by Leenaarts et al. (2006b). Such MC brightenings are more familiar as "facular bright points" in the continuum and in the molecular G-band around 4305 Å and as "line gaps" in neutral metal lines, but it actually reaches the largest contrast in the blue wing of Hα (Leenaarts et al. 2006a). It is well understood and is not a sign of heating but of deeper-than-normal radiation escape (see the summary and references in Rutten et al. 2013). Hence, care must be taken to ascertain that features that appear bright in an Hα wing are indeed EBs and not just facular brightenings—a warning already given by Ellerman (1917) himself. A first check is to ascertain from the daily magnetogram animations from *SDO*/HMI that the observed field of view is part of an active region with much flux emergence and fast streaming motions, including bipolar collisions.

In Paper I and Paper II we found that EBs are best identified using Hα wing images with slanted viewing away from disk center. We obtain such wing images by summing the three spectral samplings of both Hα wings around $\Delta\lambda = \pm 1.0$ Å. In limbward viewing at the SST resolution, MCs reach less Hα-wing brightness contrast than near disk center, whereas EBs appear with definite flame morphology. They appear as elongated bright upright features that rapidly flicker (hence "flames") for a few minutes while their feet are anchored in and travel along MC-rich intergranular lanes. Their tops extend intermittently up to megameter heights. This rapid-flame behavior is the best diagnostic to classify an Hα wing brightening[4] as an EB.

In Paper I this flame morphology was used to manually identify EBs, but in Paper II we defined automated selection criteria employing the brightness contrast, spatial extent, temporal continuity, and lifetime of candidate features in SST imaging spectroscopy sequences sampling the Hα wings. These criteria were tuned to optimally recover example EBs that had been identified visually from their time-dependent morphology, and then applied to obtain a faster, more objective, and more complete identification of EBs in each dataset.

In the present analysis we have applied these criteria to our three data sets, but with an adjustment for dataset 2 in which we lowered the thresholds to 145% brightness contrast over the field of view mean for the EB kernel and 130% for adjacent pixels, instead of the Paper II values of 155% and 140%. We did so because visual inspection showed that with the latter thresholds we missed a number of features that the morphology suggested were EBs, even though they were weak in relative Hα wing excess. A reason for this may be that this field of view contained no dark umbrae or pores and therefore had a higher mean profile than in Paper II. Also, it was the closest to the disk center where MCs appear brightest in the Hα wings.

[4] We emphatically invite the reader to inspect the high-resolution EB animations available in Paper I and become familiar with this defining morphology.

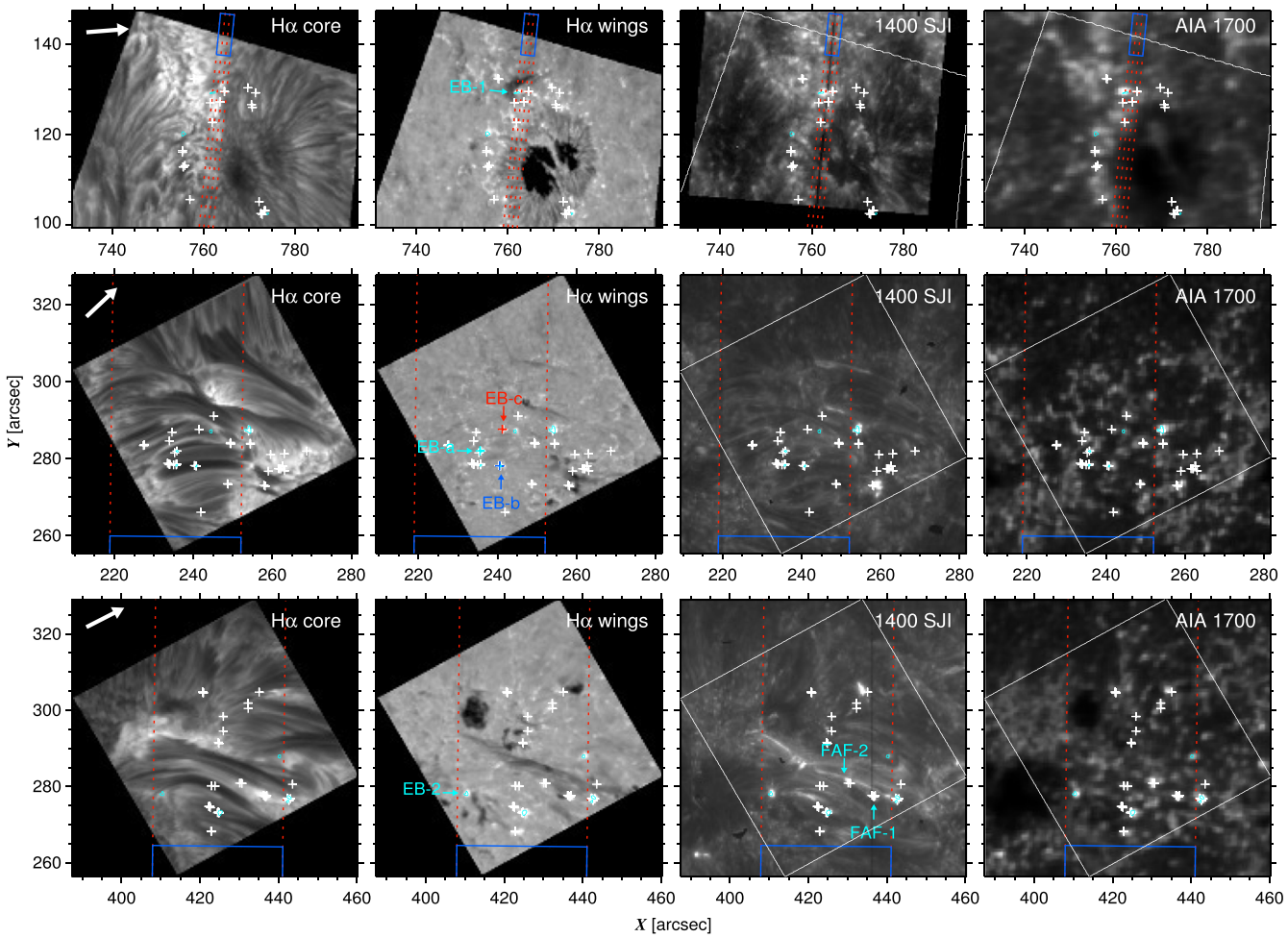

Figure 1. Field of view images from data sets 1–3 in rows from top to bottom. The SST and *IRIS* images have been rotated to solar (X, Y) coordinates. Left to right: SST Hα core, SST Hα summed wings, *IRIS* 1400 Å slitjaw (SJI = slitjaw image), AIA 1700 Å. The red dashed lines specify *IRIS* slit locations (top row) or raster extent (lower rows). Hα EB detections for the instant sampled by these images are marked with cyan contours. White plus signs mark Hα EB detections at other times in each data sequence. The selected EBs presented in detail below are identified in the second column: EB-1 in the top row, EB-2 in the bottom row, and "weak" EB-a, EB-b, and EB-c in the middle row. The position of the selected FAFs (FAF-1 and FAF-2) are indicated in the third panel of the bottom row. The white arrows in the first column specify the direction to the nearest limb. The white frames on the *IRIS* and AIA panels specify the SST field of view (the actual *IRIS* slitjaw images are larger than shown here). The blue rectangles outline the quieter areas over which *IRIS* spectra were averaged to obtain reference profiles. In the lower rows these extend 5.6 and 10.3 arcsec below the image cutouts, respectively.

(Animations a, b, and c of this figure, including *SDO*/HMI line of sight magnetograms, are available.)

Examples of the resulting threshold contours outlining EB candidates are shown in Figure 1 for those that were detected at the particular moment at which each image was taken. The numerous white plus signs mark other Hα EB detections during the entire SST observing period. Some overlap closely and are detections of repetitive EBs at about the same location.

2.4. EB Identification in the 1700 Å Continuum

In Paper II we also tried to automate finding EBs in *SDO*/AIA 1700 Å image sequences. EBs typically appear in these as strongly enhanced, fairly pointlike, and fairly stable brightness features. AIA 1600 Å images show them at yet larger brightness contrast above ordinary MCs, but as noted above the scene at this wavelength often contains FAFs as well (Rutten et al. 2013).

In the less FAF-infested 1700 Å images, a contrast criterion of 8σ above the mean intensity was found to recover most of the brighter Hα EBs. This conservative threshold may miss weaker EBs, but lower cutoff values give more confusion with non-eruptive MCs. An additional lifetime maximum of five minutes was also set to distinguish EBs from longer-lived MCs. A further non-automated check is to ignore 1700 Å detections when they exhibit FAF behavior at 1600 Å.

2.5. EB Visibility in IRIS SJI and Spectra

Blinking the *IRIS* slitjaw against the CRISP Hα animations suggested that bright EBs detected in the Hα wings often appear as bright features in the C II, Si IV, and Mg II kSJI. However, the fraction for which we also have *IRIS* spectra is small. For data set 1 this is obvious in the top row of Figure 1, where the narrow *IRIS* scan strip missed most Hα EB detections (white plus signs).

For data sets 2 and 3, the *IRIS* raster extent was much wider so that many more Hα EBs fell within it, but the slow raster repeat cadence of 516 s meant that most of these were not sampled spectroscopically during their brief lifetimes. Nevertheless, in the few cases of proper EB slit coverage, the *IRIS* spectra show corresponding brightening of the major *IRIS*

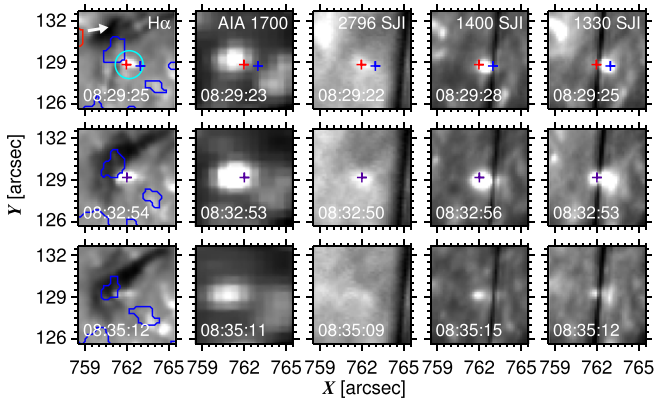

Figure 2. Time evolution of EB-1 in various diagnostics. Left to right: co-spatial image cutouts of CRISP Hα wings, AIA 1700 Å, *IRIS* Mg II k, Si IV, and C II slitjaws. The red and blue contours in the first column indicate patches of positive and negative polarity (thresholded at 0 and −1000 counts), respectively, based on the HMI line of sight magnetic field data. The time of observation is specified at the bottom of each panel. The plus signs mark the locations for which corresponding spectra are shown with the same color coding in Figure 4. The cyan circle indicates the size (and instantaneous location) of the mask used to determine the light curves in Figure 3. The arrow in the same panel specifies the "upright" direction to the nearest limb. The panels in each column have been byte-scaled to the same extremes.

lines, so that it is probable that the slitjaw brightenings are simply set by the wavelength-integrated enhancements of these lines.

Examples are shown in Figure 1 and are yet clearer in the smaller cutout sequences in Figures 2, 6, and 9 discussed below. In general, the bright *IRIS* slitjaw features are not one-to-one identical with the Hα-wing brightenings, but there is good overall correspondence in location, orientation, shape, and evolution.

2.6. EB and FAF Selection for Presentation Here

For dataset 1 application of the Paper II Hα criteria resulted in 31 Hα EB detections, many of which showed pronounced slitjaw brightening. However, of those 31 Hα EBs, only 4 where sampled by the *IRIS* slit and only 1 of these showed pronounced brightening in the slitjaws. We selected the latter one for detailed presentation below and henceforth refer to this EB as EB-1. It also passed the 1700 Å criteria of Paper II, while the other three sampled by the *IRIS* slits did not.

Dataset 2 was the closest to the disk center so that distinction from ordinary MCs and recognition of flame morphology was likely hampered by top-down viewing. Our down-tuned Hα criteria gave 49 EB detections, of which 6 were sampled spectroscopically by *IRIS*. Most were weak in Hα and the *IRIS* spectra, and weak or invisible in the *IRIS* slitjaws. We selected the three with the highest *IRIS* profiles and call them EB-a, EB-b, EB-c henceforth and present their spectra below as examples of weaker or even questionable EBs. Only EB-b passed the 1700 Å criteria.

For dataset 3, the Paper II Hα criteria yielded 56 detections, of which 10 were sampled spectroscopically by *IRIS*. Most were weak; the exception was a very long-lived repetitive EB, which we call EB-2 henceforth. It did not pass the Paper II 1700 Å criteria initially, but passed when we relaxed the constraint on lifetime to distinguish weak EBs from longer-lived MCs. EB-2 was clearly not a pseudo-EB in Hα. In 1700 Å it occurred repetitively for an exceptionally long period of time.

In dataset 3 we also noted a string of fierce repetitive interconnected brightenings of which the *SDO*/AIA 1600 Å animation shows they were FAFs. We also selected two of these for comparative display and discussion below.

A fourth SST-*IRIS* dataset taken on 2013 September 25 was discarded because only 1 of its 48 Hα EB detections was sampled by *IRIS*. It did not show up in the SJI and produced only slight ultraviolet line brightenings, much as the discarded EBs in dataset 2 and therefore, like those, not selected for detailed presentation here. There were more EBs visible in the latter, but outside the narrow raster strip.

3. RESULTS

In this section we present the observations for each selected feature in succession using the same plot formats for cutout samples from the SST, *SDO,* and *IRIS* SJI, light curves distilled from these, and *IRIS* spectra at selected pixels and times corresponding to the cutouts. For each feature we add some interpretation, but we postpone overall discussion to Section 4.

3.1. Details for EB-1

When viewing EB-1 in the Hα sequences, using CRISPEX to inspect its spatial, temporal, and spectral behavior in flexible cursor-controlled animation mode (a recommended modus operandi), this EB appears as a sequence of unmistakable tall EB flames in the outer Hα wings, re-occurring in rapid succession during the entire observing period, with fast motion of its successive footpoints away from the spot along an MC-filled lane. Our CRISPEX inspection also showed that a dark redshifted chromospheric fibril was overlying the Hα core part of the time.

In the AIA 1700 Å sequence EB-1 also stands out as bright and EB-like, i.e., pointlike, roughly stationary, and without filamentary FAF signature. The HMI magnetogram sequence shows that it occurred in a complex region with much streaming motion from the sunspot toward the extended plage and pores of both polarities further north. Small patches of opposite polarity traveled fast in this flow but were barely visible with HMI. Such patches likely produced EB-1 successively while canceling. In Paper II we observed EBs at similar cancelations of small opposite-polarity patches in SST magnetograms with better detail than given by HMI.

Unfortunately, EB-1 was sampled by the *IRIS* slit only at the beginning of the SST sequence and only at two positions of the narrow scan pattern. In its successive flarings, EB-1 migrated eastward out of the scan strip. However, during this 10 minute overlap period, the rapid-scan format gave good temporal sample resolution.

Figure 2 shows a selection of small-field cutouts of EB-1 in various diagnostics. The time differences along rows are negligible by using nearest-neighbor selection, whereas the rows are about three minutes apart in order to sample EB-1's evolution. Colored plus signs specify the pixels for which *IRIS* spectra are shown in Figure 4 with the same colors. The slitjaws in the last two columns of Figure 2 show the *IRIS* slit as a dark near-vertical stripe at or close to the plus signs at corresponding times.

EB-1 appeared to be fairly upright, so that the red and blue pixels in the top row of Figure 2 likely sampled its lower and

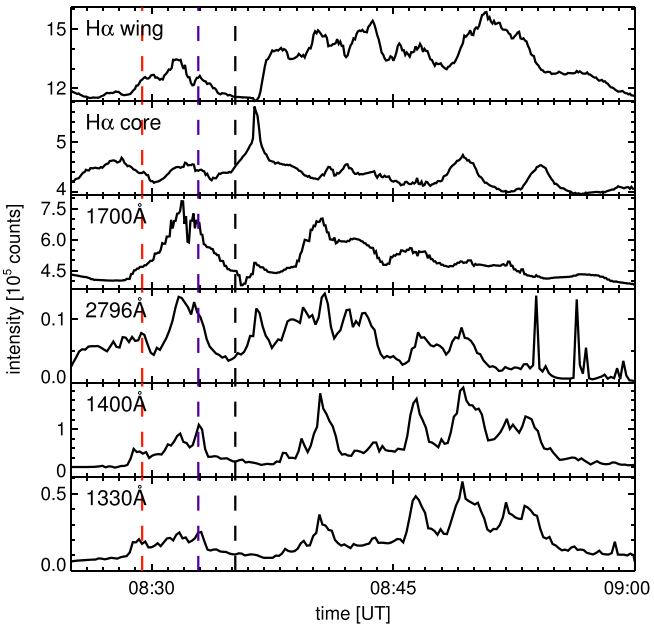

Figure 3. Light curves for EB-1 showing, from top to bottom, the intensities in the Hα wings and core, AIA 1700 Å, and the Mg II k, Si IV and C II slitjaws as function of time. Each intensity value is the sum over a co-moving circular aperture centered on the Hα detection with a diameter of 2.0 arcsec (1.5 times the maximum diameter of the Hα EB contour), as indicated by the circle in the first panel of Figure 2. The presence of the slit and diffraction from it produced extra modulation of the lower three diagnostics during the first 10 minutes. The vertical dashed lines mark the times per row of Figure 2, with the same color coding. The first (red) corresponds to the near-simultaneous blue and red sampling of EB-1 in the first row; the second to the violet colored sampling in the second row; and the third (black) to the EB aftermath in the third row for which we show no *IRIS* spectra (since not of interest).

upper parts (the spectra in Figure 4 confirm this distinction). The violet pixel in the second row of Figure 2 sampled the same location on the Sun as the red pixel in the first row, but during the 2.5 minutes between these samplings EB-1 moved to the left in its successive flaring, so that the violet pixel sampled its middle part. The morphology of the emission patches in Figure 2 suggests that the 1700 Å feature came mostly from the lower part and that the ultraviolet images sampled increasingly more of the upper part for higher formation temperature (left to right). The Hα-wing brightness maps only the lower part in the top row, but in the second row EB-1 appears as an Hα-wing brightness patch that resembles the ultraviolet patches, whereas the 1700 Å feature remained dominated by the lower part.

The row-to-row evolution in Figure 2 suggests that EB-1 grew from the first sample time to the second, while migrating leftward, and then diminished. This is confirmed by Figure 3 which shows the time behavior of the integrated emission of EB-1 in the SST, *IRIS*, and *SDO*/AIA imaging. The integration area was defined appreciably wider than the Hα detection contour to admit the larger extent of the brightenings in the *IRIS* slitjaw and AIA images (Figure 2). The first part covers the three sample times of Figure 2 (dashed vertical lines) and shows a rise, a high peak around 08:32 UT, and a subsequent decay in all diagnostics. Subsequently, there were even more brightenings, with interesting differences between the various curves, but unfortunately without spectroscopic sampling by *IRIS* because EB-1 had drifted off the slit scan strip. The Hα-core curve shows a high peak a minute after the third sampling. Inspection showed that it was from a bright fibril ending of the type commonly seen at Hα line center, with many similar ones in the neighborhood; as can be seen, it was nothing like the microflare of FAF-1 discussed below.

Figure 4 shows SST Hα profiles and *IRIS* ultraviolet line profiles of EB-1. The color coding corresponds to the pixel markers in Figure 2. The black profiles are the spatial average over the area specified by blue frames in Figure 1. These reference profiles serve to gauge the amount of unusual brightening in the EB profiles.

In the first panel of Figure 4 the red Hα profile from the lower part of EB-1 shows a characteristic EB signature: excessive wing intensity but nothing special in the core. The blue profile from the upper part shows no Hα brightening yet, as already noted in the first row of Figure 2, but the subsequent violet profile shows considerable Hα wing brightening. This profile also indicates significant core redshift, but this we attribute to the overlying fibril seen in the line-center animation. EB-1 contributed only the wing parts outside the steep core flanks.

If overlying fibrils are opaque in the Hα core, they must be much more opaque in Mg II h & k for the following reasons. In Paper II we found that the core of Ca II 8542 Å is affected by overlying fibrils similar to Hα, although with larger sensitivity to non-thermal Dopplershifts. Fibrils that appear opaque in both Hα and Ca II 8542 Å must necessarily be yet more opaque at the centers of the Ca II H & K lines, since these are from the Ca II ground state while the 8542 Å line is from an excited level. Such fibrils must then be 18 times (Mg/Ca abundance ratio) more opaque yet at the centers of the Mg II h & k lines.

The Mg II h & k cores in the bottom right panel of Figure 4 indeed show only a small response and the 2796 Å SJI in Figure 2 show less EB brightening than the other diagnostics. However, overlying fibrils must also become transparent further out in the h & k wings, just as in the Hα wings. The violet h & k profiles in Figure 4 indeed show outer wing brightening. The 2796 Å light curve in Figure 3 shows a peak around 08:32 UT from these broader Mg II k wings.

In contrast to the fibril-dominated Hα and Mg II h & k cores, there is large response to EB-1 in the Si IV and C II profiles in Figure 4 and also in the Mg II triplet lines between h & k. They all show a clear progression of excess emission for the red, blue, and violet samplings, again suggesting that the upper part of EB-1 was hotter than the lower part and became hotter with time. From red to blue the C II lines also became much wider. Only their central self-absorption dips remained unaffected. These are probably also fibrilar.

In addition to this brightening, the profiles of all these lines show marked asymmetries with very good correspondence between them. The redshifts of the red profiles from the lower part suggest downflow, while the blueshifts of the blue and violet profiles from the upper part suggest upflow. These patterns provide direct evidence for the presence of a bi-directional flow, as discussed earlier for EBs by Shibata et al. (2007), Matsumoto et al. (2008), Archontis & Hood (2009), and in Paper I.

The blue Si IV peaks show blueshifts of roughly 30 km s^{-1}. More precise fits with double Gaussians to reproduce their asymmetry gave blueshift magnitudes of about 45 km s^{-1} for the main (i.e., highest intensity) components. The violet Si IV peaks for the later sampling show smaller blueshifts

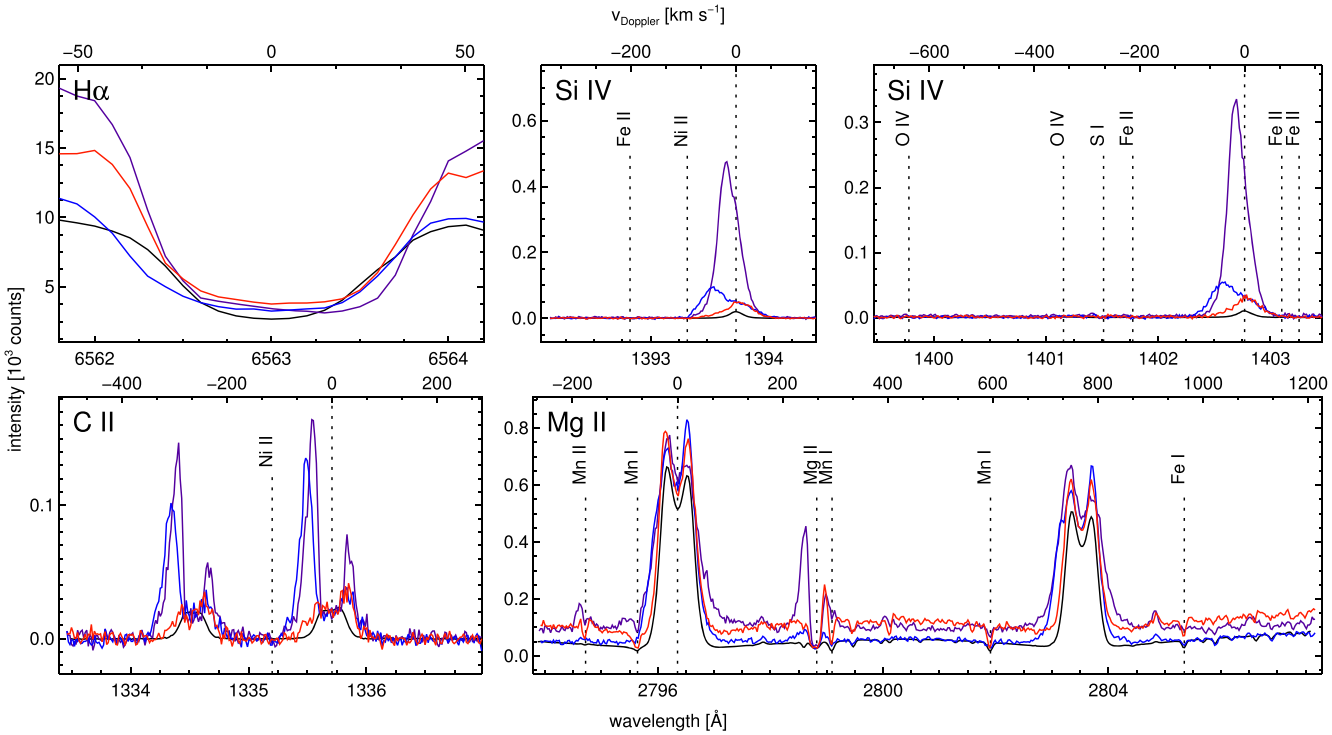

Figure 4. CRISP and *IRIS* spectra of EB-1. Clockwise: Hα, the Si IV lines near 1394 and 1403 Å, the Mg II h & k lines near 2796 and 2804 Å with the (double) Mg II triplet lines near 2798 Å between them, and the C II doublet near 1335 Å. Several other lines and blends are indicated by the labeled vertical dashed lines. All wavelengths are vacuum values (against the convention of specifying air wavelengths above 2000 Å because *IRIS* is a space platform). The red profiles were taken at 08:29:25 UT, the blue profiles at 08:29:28 UT, and the violet profiles at 08:32:53 UT. The colors correspond to the pixel markers in Figure 2. The black profiles show the average spectrum for the "quiet-Sun" reference box in the first row of Figure 1. Axes: intensities in instrument units vs. wavelengths in Å, with equivalent Dopplershift from line center of the strongest line along the panel tops. The second Si IV line (third panel) is drawn at a doubled intensity scale to offset the factor of two between their transition probabilities; equal apparent profile heights indicate optically thin line formation.

(about 15 km s^{-1}), but this was the middle part of the EB, not its top, due to its eastward progression (Figure 2).

Thus, there is no point in inspecting (or modeling) the cores of Hα and Mg II h & k to study EB behavior, but the striking agreement in Doppler asymmetries for the Mg II triplet, Si IV, and C II lines suggests that these sample the underlying EB without fibrilar obscuration. These *IRIS* lines thus provide diagnostics in which EBs are "unveiled."

In addition, these EB-unveiling diagnostics differ clearly in how they sample EB-1. The Si IV lines indicate a roughly optically thin feature for the red and blue profiles even at their centers, because each pair reaches similar heights in the second and third panels of Figure 4 and shows no flattening or dip in the line cores. Since the plot scales of the Si IV panels differ by the transition probability ratio, such apparent height equality suggests optically thin formation. For the violet profiles this is not the case, suggesting that the increased emissivity went together with larger EB-1 opacity.

This thickness measure is quantified in Figure 5 which plots the intensity of one Si IV peak against the peak ratio. They were measured by averaging the profiles over all spatial-temporal samplings of pixels within the bright EB-1 patch in the 1400 Å SJI that correspond to each successive *IRIS* scan, and smoothing the top of each averaged profile to measure its maximum intensity.

For an optically thin cloud without background irradiation, the emergent doublet intensities equal the local emissivities times the geometrical thickness and obey the transition probability ratio of 2. For thicker features the ratio reduces, reaching unity for an opaque cloud with constant source

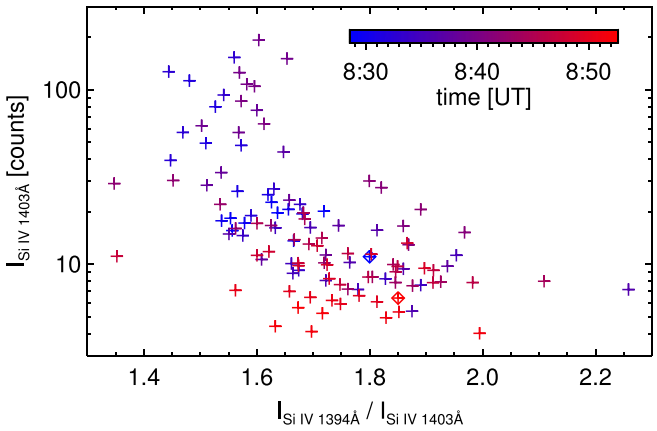

Figure 5. Peak intensity of the Si IV 1403 Å profile against its ratio with the peak intensity of the Si IV 1394 Å profile for all spectral samplings of EB-1. The color coding specifies observation time. The two diamonds specify the start and end samplings.

function and then yielding flat-topped profiles (Figure 2.2 of Rutten 2003). Figure 5 suggests that EB-1 was mostly neither thin nor thick, but "thinish" with ratio values between 1.9 and 1.5 that typically correspond to thicknesses 0.3 and 1.6, respectively. The sample time coding (color) suggests that EB-1 started and ended optically thin, but was generally somewhat thicker at high peak intensities in between.

When such features become much thicker than the photon mean-free path, internal resonance scattering tends to cause

outward source function decline and a corresponding central profile dip that is commonly called self-absorption. Such dips are seen in the C II lines and also in the Mg II triplet lines. However, their peak heights and asymmetries correspond very well to the Si IV profiles. Their peaks rise in concert and the higher peak of each profile is on the side to which the Si IV peaks are shifted. This good correspondence also suggests that these peaks sampled EB-1 without obscuration from overlying fibrils. The latter caused only the central dips because these show no Dopplershifts. Since the outer wings still show about similar intensities as a function of wavelength separation from the line centers, the peaks and wings seem to sample the EB in an optically thick fashion (otherwise they would also differ a factor of two, the transition probability ratio). For an optically thick feature the profiles represent Eddington–Barbier mapping of the source function at monochromatic optical depth $\tau_\lambda = 1$. In this case the different Dopplershifts of the upper and lower parts of EB-1 affect the optical depth scaling and produce the peak asymmetries. Thus, these unveiled *IRIS* diagnostics provide both thin and thick EB sampling.

The final features of interest in Figure 4 are the line blends. The Si IV and C II lines are too narrow to reach the nearby Fe II and Ni II lines (rest wavelengths indicated by dashed vertical lines), but the blue wing of Mg II k and the raised overlapping wings between h & k contain strong Mn I absorption blends at 2795.64, 2799.09, and 2801.91 Å in the red sampling of the lower part (best seen by zooming in). They are weak or absent in the other samplings. We attribute them to foreground upper photosphere gas crossed by the slanted line of sight toward EB-1 that is not part of the phenomenon and indeed imparts no obvious Dopplershift. A line of sight to the lower part then passes through the Mn I formation layer, while a line of sight toward the upper part catches less or none of it.

The Mn II blend at 2794.72 Å appears with interesting profiles: as a self-reversed line in the red sampling of the lower part, absent in the blue sampling of the upper part, but appearing with a blue-peaked profile similar to the Mg II triplet lines at 2798.82 Å in the later violet sampling of the upper part. This similarity indicates sampling of the EB itself.

In summary, the *IRIS* diagnostics provide an informative, understandable, and self-consistent view of EB-1 that fits very well with our earlier EB descriptions. EB-1 appeared as a photospheric below-the-fibrilar-canopy heating event with upward progression with time, larger heating higher up, and unmistakable bi-directional jet signature.

Are these EB spectra similar to the IB spectra of Peter et al. (2014)? While the C II and Si IV lines do show brightening, also with bi-directional Dopplershift signatures, their wings are not extravagantly wide. This may be a matter of timing. It is a pity that *IRIS* did not sample its aftermath, as is demonstrated by the next example.

3.2. Details for EB-2

EB-2 was sampled in *IRIS* spectroscopy during a longer period, but only intermittently due to the slow raster repeat at 8.6-minute cadence. Figures 6–8 display results for EB-2 in the same format as Figures 2–4. This EB had the advantage that it appeared aligned along the *IRIS* slit, so that its top and bottom were spectroscopically sampled at the same time in each row of Figure 6. The alignment was fortuitous since EB-2 was tilted

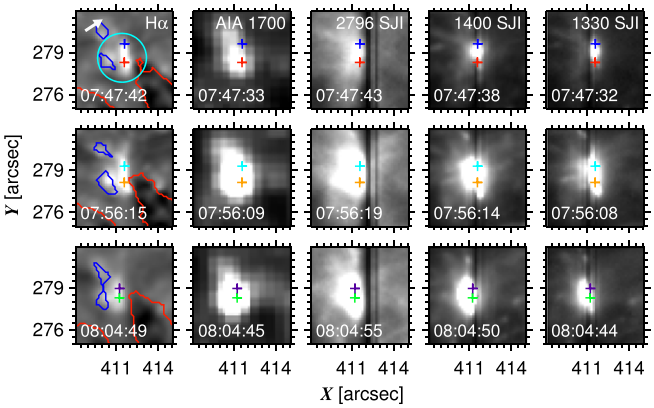

Figure 6. Time evolution of EB-2 in the format of Figure 2, except that the red and blue contours in the first column are based on CRISP Fe I 6302 Å Stokes *V* data (thresholded at ±450 counts). In each panel the pair of pixel markers specifies the sample locations of simultaneously recorded spectra shown in Figure 8. The temporal separation between rows is about eight minutes, larger than in Figure 2. It corresponds to successive *IRIS* rasters.

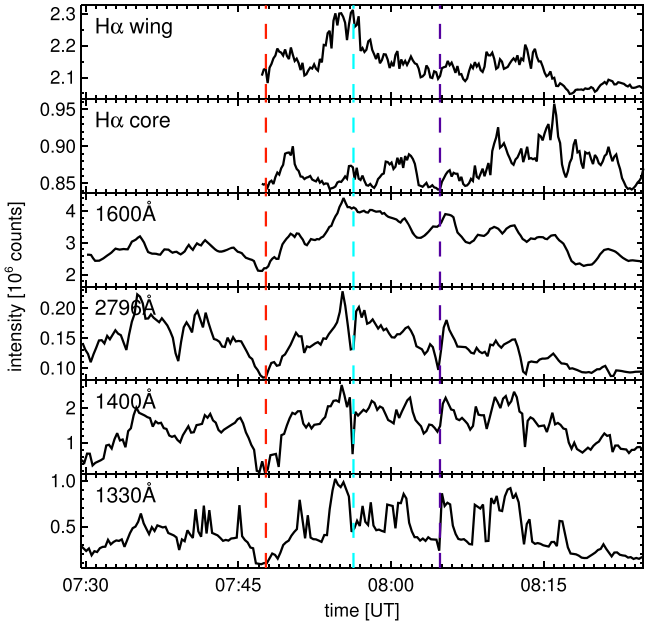

Figure 7. Light curves for EB-2 in the format of Figure 3. In this case, the integration aperture had a diameter of 3.5 arcsec (1.5 times the maximum diameter of the Hα EB detection contour), as indicated in the first panel of Figure 6. The three dashed vertical lines correspond to the sampling times of the three rows in Figure 6. There are corresponding dips in the lower three curves from the slit presence over the feature.

considerably away from the local vertical in its azimuthal orientation (angle with the arrow in the first panel of Figure 6).

Inspection of the SST Hα sequences showed an unmistakable large, repetitive EB flame. EB-2 was already present at the start of the SST observations at 07:47 UT, quickly brightened, and remained nearly continuously present in the AIA image and *IRIS* slitjaw sequences until 08:29 UT. These image sequences and the corresponding light curves in Figure 7 suggest that there was also preceding EB activity during 15 minutes before the SST start. A longer-duration AIA 1700 Å sequence suggests strong repetitive EB activity at the same location from 06:36 UT onward. The HMI magnetogram sequence shows very fast streaming with an extended patch of white polarity running into a fairly large patch of black polarity

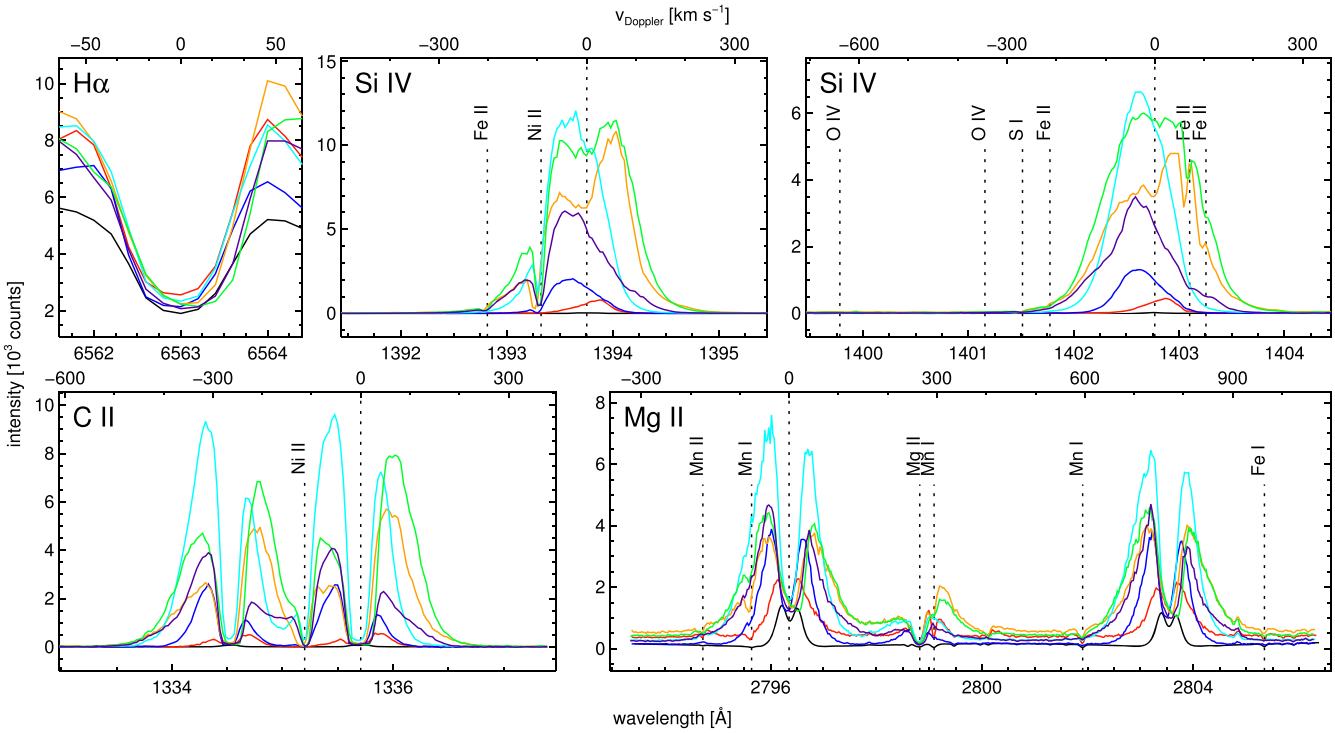

Figure 8. CRISP and *IRIS* spectra of EB-2 at the marker positions in Figure 6, with the same color coding. The red and blue profiles were taken at 07:47:38 UT, the orange and cyan profiles at 07:56:14 UT, and the green and violet profiles at 08:04:45 UT. The format is the same as for Figure 4, except that the Hα panel is compressed in wavelength to make place for wider Si IV 1394 Å profiles conserving their Doppler velocity scale.

that vanished gradually and was gone by 08:30 UT. The SST magnetograms have higher spatial resolution but only at the best seeing moments; the homogeneity of the HMI sequence makes it more suited to follow such pattern changes.

The hotter AIA diagnostics (304, 171, 193 Å) show no especially interesting activity occurring at the site of EB-2 during the entire period. EB-2 thus seems a bona fide EB, but repeating over unusual duration due to the continued supply of opposite-polarity fields.

The top row of Figure 6 with red and blue pixel markers shows EB-2 at the start of the SST observations (the first vertical line in Figure 7). The corresponding red and blue Si IV and C II profiles in Figure 8 appear similar in shape to those in Figure 4, but note the differences in intensity scales: the blue and red Si IV profiles reach count values nearly 20 times higher than for EB-1, more than expected from the doubled exposure time. They are also much wider. The red C II profiles are still well separated, but the blue profiles nearly overlap. This is not seen in quiet-Sun spectra (Lites et al. 1978).

The red and blue profiles nevertheless still display similar profiles as EB-1: clean humps with the blue ones from the upper part reaching higher intensities than the red ones from the lower part, and with redshifts for the lower sampling and blueshifts for the upper sampling that again correspond very well between the Si IV, C II, and Mg II triplet lines. As in EB-1, the 1700 Å brightness patch in the top row of Figure 6 favors the bottom part of EB-2 while the ultraviolet images indicate higher formation for hotter diagnostics. These EB-2 results are in excellent agreement with our EB-1 findings.

However, the red and blue profiles sampled only the beginning of EB-2. It became much larger and brighter afterwards (see, for example, Figures 6 and 7). Figure 8 also adds lower and upper spectral sample pairs at the times when the *IRIS* slit passed EB-2 again around 07:56 and 08:05 UT, respectively (the second and third rows of Figure 6, with orange and cyan lower/upper markers in the second row and green and violet lower/upper markers in the third row). The Si IV and C II lines grew considerably in intensity and developed more complex profiles that do show IB signatures: wide wings, cores with complex structure, and deep blends.

The orange and green samplings of the lower part show the most complex double-peaked Si IV profiles in Figure 8. These profiles come closest in shape to the double-peaked profiles in Peter et al. (2014), which were interpreted as a signature of a bi-directional jet. Here, the small Si IV line-center dips may represent self-absorption in stationary gas, but also just a lack of stationary gas in the optically thin emissivity mapping of two counter streams as blue- and redshifted profile humps. In contrast to the similarity of the two Si IV profiles in Peter et al. (2014), the green and orange Si IV profiles of EB-2 differ between the two lines.

The Dopplershift patterns are again consistent between the different unveiled diagnostics. All samples of the lower part (red, orange, green) show redshifts domination, while the samples of the upper part (blue, cyan, violet) show single blueshifted peaks, although with redward profile tails. Most profiles show ragged tops. Such core raggedness is further discussed in Section 4.

The Ni II blends at 1393.32 Å in the stronger Si IV line and at 1335.20 Å between the C II lines are very pronounced in all but the red samplings. The Fe II blends at 1403.10 Å and 1403.26 Å in the red wing of the weaker Si IV line are present in the lower orange and green samplings, and weakly in the final upper violet sampling. These blends generally show blueshifts, which are larger in the orange than in the subsequent

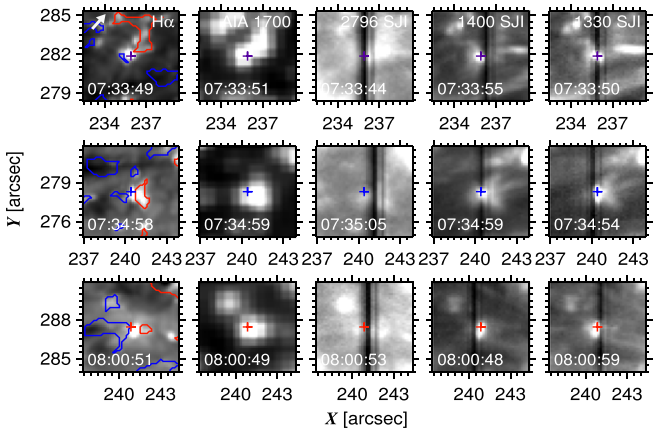

Figure 9. Image cutouts for EB-a (top row), EB-b (middle row), and EB-c (bottom row). The format is the same as for Figure 6, except that the rows are for different locations and all panels were therefore byte-scaled individually. The red and blue polarity contours represent thresholds of +100 and −250 counts, respectively.

green sampling. They suggest an upward and decelerating motion of cool gas along the line of sight to the EB.

The three lower samples (red, orange, green) show the Mn I blends in the Mg II h & k wings, which are strongest in the earlier red lower sampling, whereas they are not present in the three upper samplings. We again attribute these blends to undisturbed upper photosphere gas along slanted lines of sight to the EB foot, with lines of sight toward the upper part passing over the Mn I formation layer. In this case, the Mn II line is only weakly present in the lower samplings, without EB sampling.

The core of Hα remained similar in the various samplings, again indicating domination by overlying fibrils. The same holds for the line-center dips of Mg II h & k. The green Hα and h & k cores show similar redshift.

The Mg II h & k peaks brightened considerably in the cyan upper sampling (the dip in the 2796 Å light curve in Figure 7 is due to the slit). This curve tracks the 1700 Å light curve fairly well. Since the peak asymmetries also correspond with those of the C II lines, the fibrilar obscuration may have been thinner for this sampling. The cyan Hα core is also relatively narrow.

The outer wings of the Mg II h & k seem to sample EB-2 in an optically thick manner because they have about equal intensities in the two lines (which also have a transition probability ratio of two).

We conclude that EB-2 showed EB-1-like profiles in its onset and later developed more outspoken IB signatures. We do not know whether EB-1 did the same, but EB-2 shows that strong EB activity can indeed produce IB-type spectra, as suggested by Peter et al. (2014).

The similarity of the orange and green lower profiles and the similarity of the cyan and violet upper profiles at an 8.6 minute sampling delay suggests that the feature persisted over long duration.

Such a hot signature was not seen at the onset of EB-2, implying that the preceding hour of EB activity suggested by the AIA 1700 Å animation had not left one by that time.

3.3. Details for EB-a, EB-b, and EB-c

EB-1 and EB-2 were well-defined strong EBs. We now turn to the weaker or questionable EB-a, EB-b, and EB-c in dataset 2. Figures 9 and 10 show their sampling and spectral profiles in the format of Figures 2 and 4.

The HMI magnetogram sequence displays a complex region with much streaming motion in which opposite-polarity patches canceled frequently. There were strong Hα EBs that appeared as obvious 1700 Å ones, but these were unfortunately not sampled by *IRIS*. As noted above, we lowered the Hα discrimination level to include weaker events that were sampled by *IRIS* because their Hα morphology indicated EB nature rather than MC nature, although such recognition was hampered by more vertical viewing than in data sets 1 and 3. In the AIA 1700 Å animation none of these appeared as an obvious EB (even though EB-b passed the Paper II 1700 Å criteria). For example, in the first two panels of Figure 9 the Hα feature appears EB-like, but the neighboring normal MCs appear as bright in 1700 Å.

The three EBs we selected for display are the ones with the highest intensities in the Si IV lines. They are sufficiently high to confirm that these candidates were not pseudo-EBs (ordinary MCs; if they were, *IRIS* would show such profiles from network everywhere). We therefore present these as non-suspect but weak EBs.

In Figure 10 the Si IV lines reach values about twice as high as those for EB-1 in Figure 4, which could be explained by the doubled exposure time, but these Si IV profiles are more complex. The apparent Si IV height equality between the differently scaled panels again indicates thinish formation, with the non-Gaussian shapes suggesting viewing through multiple Dopplershifted components. This strengthens our judgments from Paper I and Paper II that slanted EB viewing helps to diagnose EB formation. In Figures 4 and 8 it did by spatially separating the different Dopplershift signatures of the lower and upper parts of the bi-directional jet. Here, these likely mixed together along the line of sight in all three EBs.

Thus, the Si IV profiles in Figure 10 suggest that the line of sight sampled both a blueshifted upper part and a redshifted lower part, with the upper part again hotter for EB-b (blue profiles) but with about equal contributions for the other two. All Si IV cores show small-scale raggedness (Section 4).

The C II profiles are similar to those of EB-1 in Figure 4 but with closer peak equalities that again suggest bi-modal sampling. For EB-b, the blue profile of the Mg II triplet lines shows opposite asymmetry to the blue Si IV and C II profiles, suggesting a peak formation in the lower part similar to the three lower samples of EB-2 in this line in Figure 8.

The various blends are markedly present in all three samplings. The Fe II and Ni II blends again show substantial blueshifts, while the Mn I and Mn II lines in the last panel show none. In top-down viewing as suggested by the jet mixing, the latter must be from cool upper-photosphere-like gas above the EBs, suggesting that the EB flames did not reach high into the atmosphere.

The upshot is that these three weak EBs adhere to the pattern set by EB-1 and EB-2 in their beginning phases, but without spatially resolving the bi-directional jets. It is better to observe EBs away from disk center, which also increases EB contrasts over MCs at 1700 Å.

3.4. Details for FAF-1

In dataset 3 a string of very bright FAFs appeared in the lower part of the field of view in Figure 1, east of EB-2. We

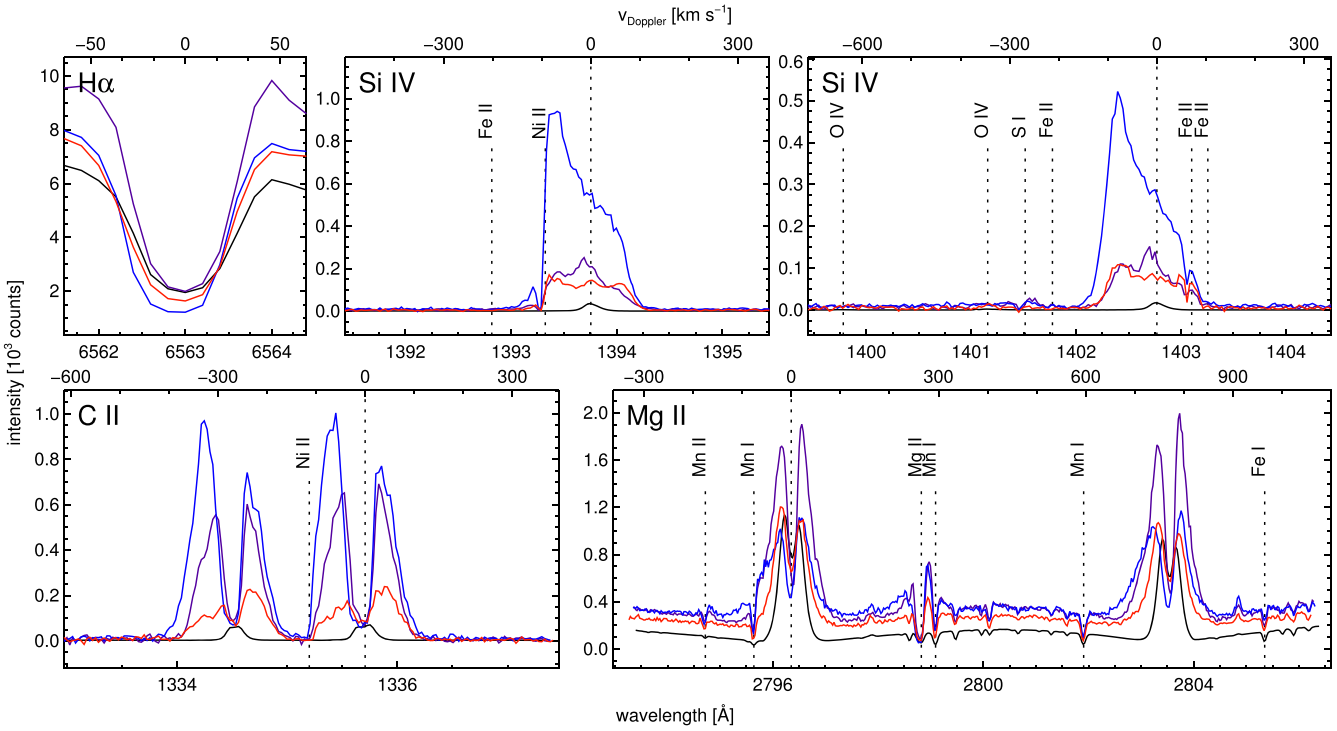

Figure 10. CRISP and *IRIS* spectra of EB-a (violet), EB-b (blue), and EB-c (red) in dataset 2 at the marker positions in Figure 9 and with the same color coding. The format is the same as for Figure 4.

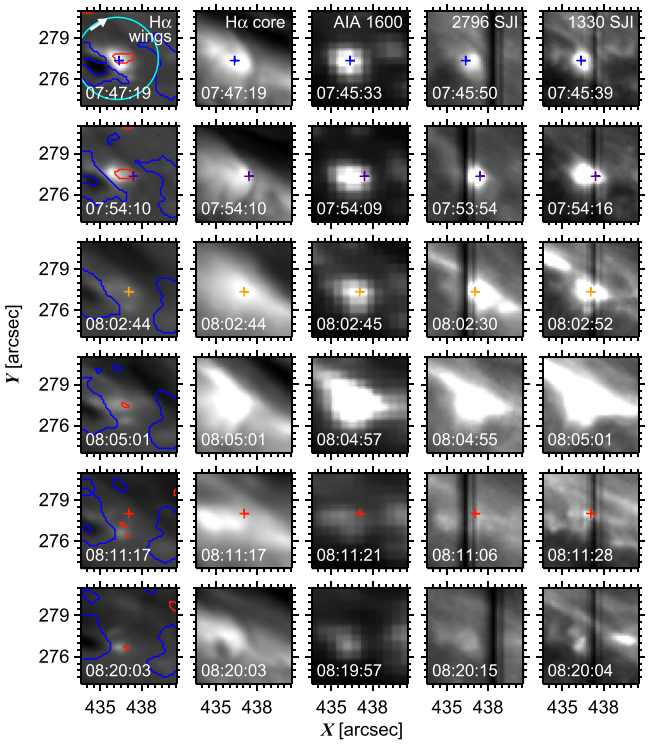

Figure 11. Image cutouts for FAF-1. The format is the same as for Figure 6, except that SST Hα core images are added in the second column, AIA 1600 Å images instead of 1700 Å images are shown in the third column, and no 1400 Å slitjaw images are shown because they were all nearly identical to the 1330 Å ones. The red and blue polarity contours represent thresholds of +100 and −450 counts, respectively. The sample times correspond to 5 successive (8.6 minutes apart) slit samplings of this location in the *IRIS* raster pattern, plus the moment of the Hα microflare (fourth row). The byte-scaling is the same along columns.

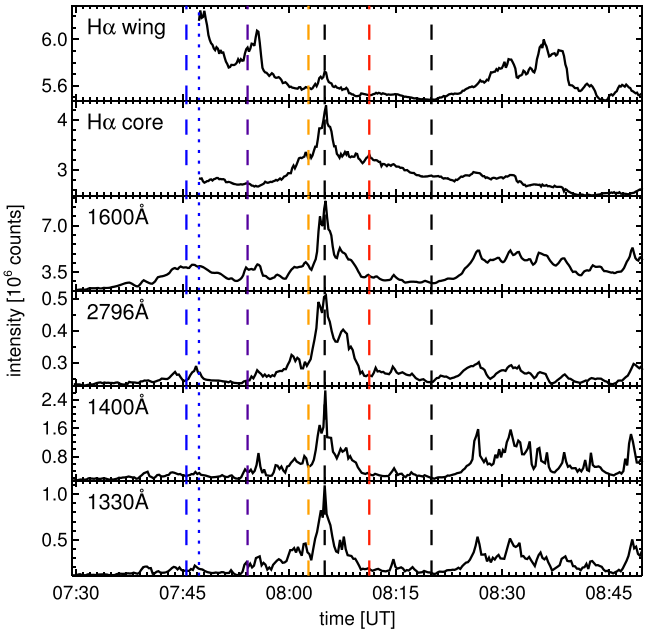

Figure 12. Light curves for FAF-1 in the same format as Figure 3. The integration aperture had a diameter of 6.0 arcsec, as indicated in the first panel of Figure 11. The vertical lines correspond to the sampling times of the rows in Figure 11. The dotted one is for the first Hα sampling, slightly offset from the first *IRIS* sampling because the SST observation started at 07:47 UT.

selected two for display in Figures 11–16. Their locations are specified in Figure 1.

Blinking the AIA 1700 Å against HMI magnetogram animations shows that FAF-1 started when a small patch of black polarity ran fast from afar to merge with a larger black one adjacent to yet a larger patch of white polarity; all black

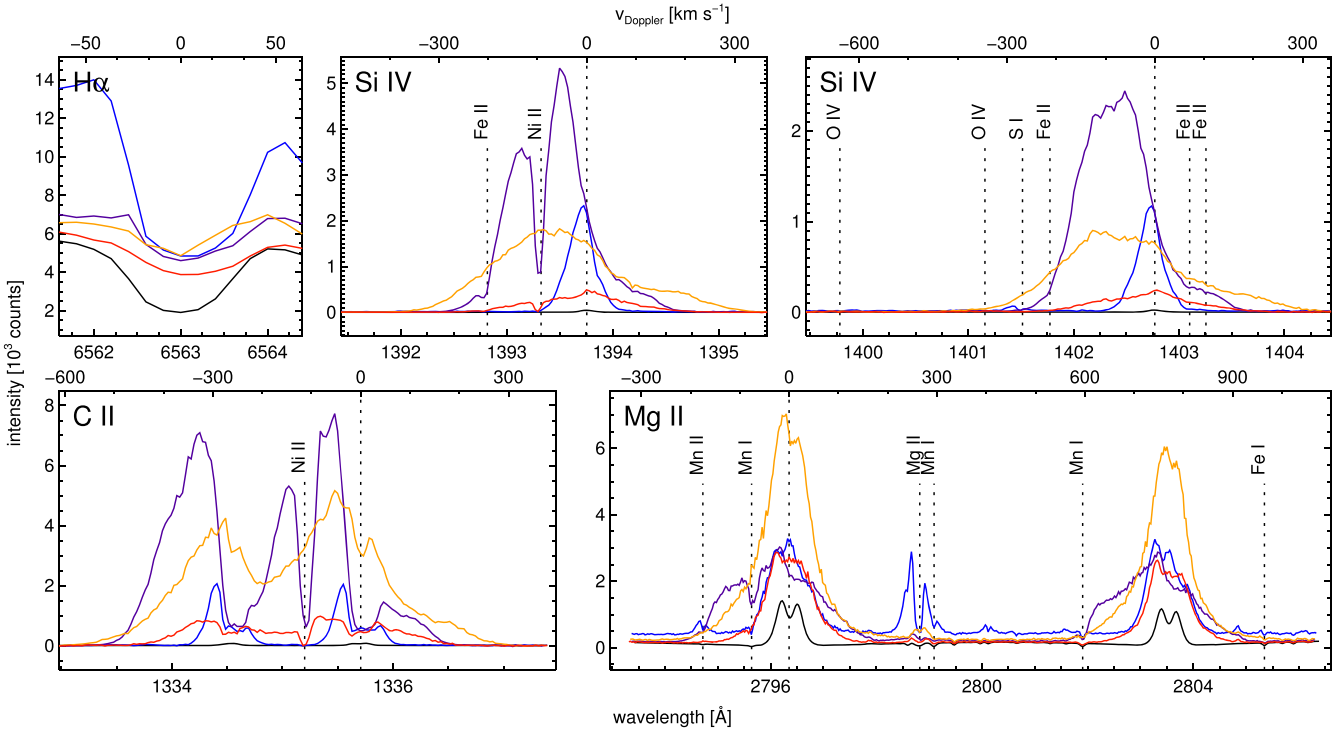

Figure 13. CRISP and *IRIS* spectra of FAF-1 at the pixels marked in Figure 11. Format as for Figure 4.

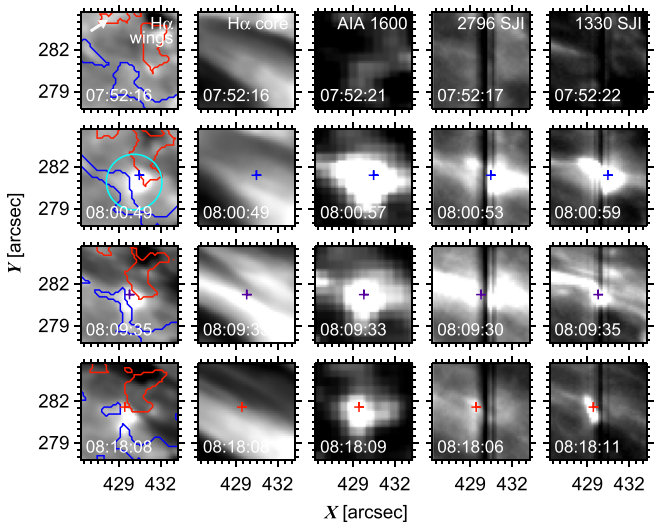

Figure 14. Image cutouts for FAF-2 in the format of Figure 11, with opposite-polarity contours at thresholds of ±500 counts.

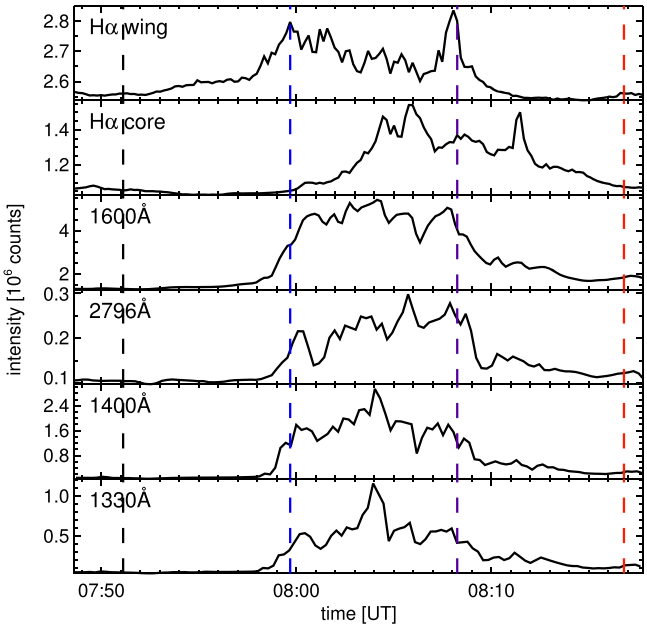

Figure 15. Light curves for FAF-2 in the same format as Figure 12. The integration aperture had a diameter of 4.0 arcsec, as indicated in the second panel of Figure 14.

polarity then vanished. FAF-2 occurred next to a fairly large black polarity patch that moved steadily east into a weak diffuse, barely visible, white polarity patch.

FAF-1 exhibited the strongest and most FAF-like flaring, at 08:05 UT. It did so not only in AIA 1600 Å but also in the Hα core, appearing as a very bright microflare. At about that moment, filamentary arch-shaped brightenings extended from it and connected to two others, FAF-2 to the northeast and another FAF to the southwest. Both then brightened in tandem. EB-2 also flared again at 08:05 UT (Figure 7), but inspection of the AIA 1600 Å animation does not suggest a filamentary connection from FAF-1.

The double filamentary arches extended at apparent speeds over the surface of 200 km s^{-1}and then around 08:10 UT gave the impression of lifting off upward in the form of a bright thin arc-shaped thread, or giving such an appearance from successive brightening of a fan of adjacent higher field loops, over a length of about 20 arcsec and with an apparent projected rise speed of about 40 km s^{-1}. This apparent liftoff was vague in AIA 1600 Å but produced a very bright arch beside FAF-1 in AIA 304, 171, and 193 Å during four minutes, with the same morphology in these diagnostics. Thus, in contrast to EBs, which do not excite response in the hotter AIA channels, FAF-1 did so very markedly.

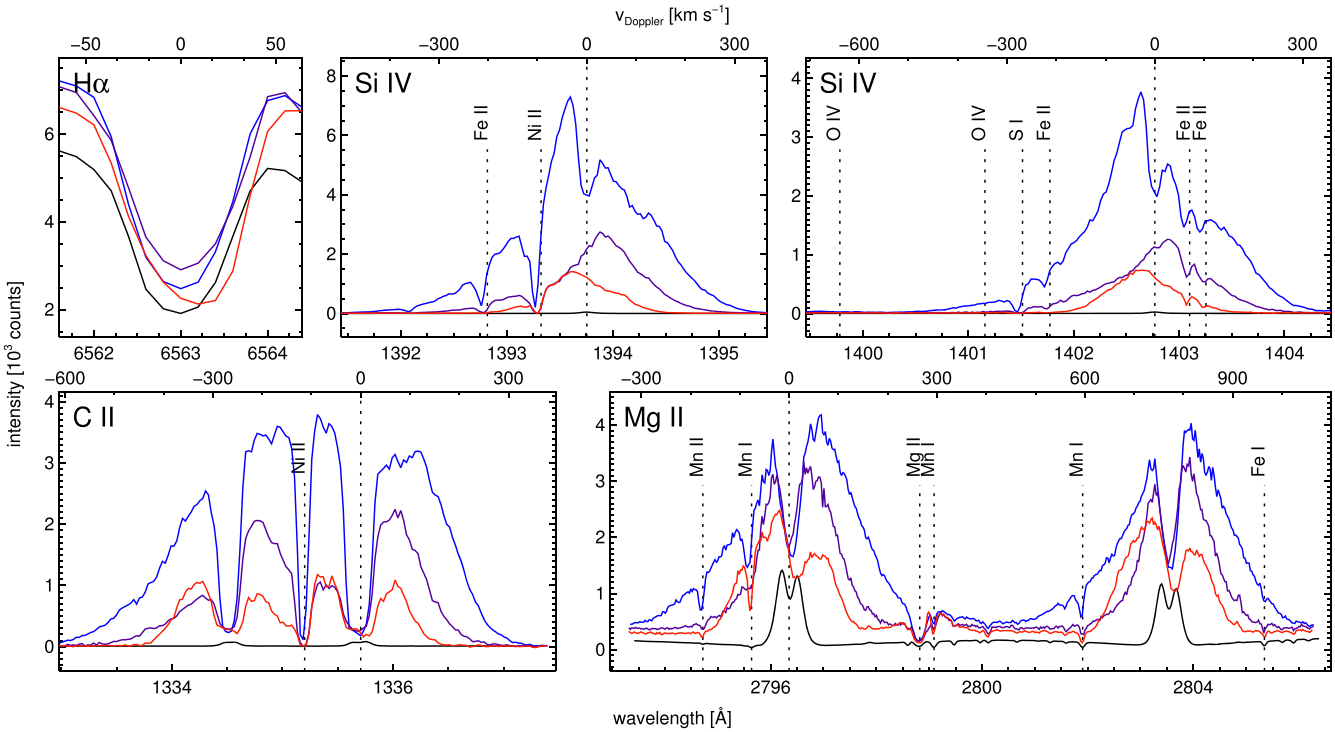

Figure 16. CRISP and *IRIS* spectra FAF-2 at the pixels marked in Figure 14. The format is the same as for Figure 4.

Inspection of the *IRIS* spectra showed no spectacular profiles from this million-Kelvin arch: the Si IV lines were enhanced but single-peaked, the C II lines enhanced and double-peaked but fairly average in width, Mg II h & k were enhanced and broadened, and there was no sign of the Mg II triplet lines. However, the O IV lines at 1399 and 1401 Å were clearly present throughout the hot arch. These signatures merit further investigation, but studying and displaying such hot coronal FAF aftermaths falls outside the scope of this EB paper. We concentrate here on the lower atmosphere signatures at the FAF-1 site.

Unfortunately, the *IRIS* slit did not sample FAF-1 at the time of its Hα flaring and filamentary extension. We therefore display the imaging at this time in the fourth row of Figure 11 and show spectra from all slit passes before and after. In the fourth row the Hα core shows its microflare while the onset of the filamentary extensions is clearest in the 1330 Å slitjaw image, but also noticeable in Hα. There was no enhancement of the Hα wings, nothing like an EB, at that time.

However, the first row of Figure 11 displays brightness patches like an EB, but with the abnormality of also appearing in the Hα core. The latter is not very bright at this initial sampling time in in Figure 12, but this is due to the presence of an extended dark fibril within the wide integration contour. The corresponding blue profiles in Figure 13 appear EB-like, rather like EB-1's violet profiles in Figure 4 but higher, also in Mg II h & k. The blue Mg II triplet profile shows very high peaks, also as for the violet sampling of EB-1.

The next sampling (second row, violet pixel and violet profiles) produced bright Si IV and C II lines. They remain less intense than the brightest from EB-2, but show extremely wide and much blueshifted profiles, top raggedness, and deep Ni II blends. The deep self-absorption dips of the C II lines remain at their rest wavelengths but the rest of the profiles are so blueshifted, as are the Si IV lines, that almost no red peaks remain. The intensity ratio of the Si IV lines still suggests thin to thinnish formation. Both Si IV lines resemble the Si IV profiles for B-2, 3, and 4 in Peter et al. (2014), while the C II lines are most alike the C II lines for B-3 and 4, suggesting that those three IBs may in fact have been FAFs.

The striking shape similarities between the C II and Si IV profiles blueward from the nominal line centers and in the red tails suggest similar sampling of FAF-1 in these parts of the C II lines, i.e., that the profile structure is mostly set by similar effects of Dopplershift, respectively, on the emissivity in optically thin formation and on the optical depth scales in optically thick formation.

The non-shifted C II core dips suggest formation (likely scattering) in a non-disturbed overlying region. The violet Mg II h & k profiles also show wide wing extensions, with the near equality of the two lines again suggesting optically thick formation. The violet Mg II triplet profile is about normal (nearly absent). The Mn I blends in the blue h & k wings are deep dips.

The next sampling, again 8.6 minutes later but still 3 minutes before the Hα microflare, produced the extraordinary orange profiles in Figure 13. The Si IV and C II lines have lower intensities, but are much wider and more symmetrical, as if smeared by enormous thermal broadening or sampling a wide distribution of very fast motions. They are appreciably blueshifted, but have extended red tails. The C II lines again appear very similar to the Si IV lines, except for the little dips at their nominal line centers suggesting minimal absorption (scattering) in undisturbed gas along the line sight. There are no absorption blends whatsoever. The profile tops are ragged.

The orange Mg II h & k profiles reach as high intensities as the brightest from EB-2 and with similar profiles but show only very small central dips, with ragged appearances. It is the only h & k sampling in all our spectra with obviously unequal wing intensities between the two lines. The cores share in this

behavior. The ratio is about 1.5. The orange C II profiles show a similar difference. It suggests that these lines sampled FAF-1 less thickly than our other EB and FAF measurements.

The Mg II triplet lines show slight emission. Together, the orange profiles suggest sampling a very hot rising event with much internal motion that was similarly sampled by the Si IV, C II, and h & k lines, with only a small amount of undisturbed gas causing dips at the C II and h & k line centers. It indeed seems an event on its way to become a bright million-Kelvin feature in the AIA diagnostics, becoming thin or thinish even in Mg II h & k.

The next *IRIS* sampling came six minutes after the Hα microflare (fifth row, red pixel, red profiles) and while the bright million-Kelvin AIA arch was present to the northeast (directly above FAF-1 it was at a height of about 6000 km and appeared projected well beyond the line of sight to FAF-1). These profiles are rather like the orange ones, but have lower intensity and are less blueshifted. They still have red tails but longer blue ones, show small C II line-center dips, have deep Ni II blends but no Fe II blends, only very weak Mn I blends, and ratios departing from optical thickness. There was no longer any specific brightening in the image cutouts, except the Hα core which shows a long post-flare tail in Figure 12. In summary, the red profiles suggest a cool-down aftermath.

In the last row of Figure 11 we also show the scene in the next *IRIS* sampling, in order to illustrate that the show was over. There was no longer anything of interest in the spectra (not shown).

3.5. Details for FAF-2

FAF-2 occurred close to FAF-1 but brightened earlier. It also showed double filamentary extensions in 1600 Å and also seemed to excite response in the hotter AIA channels: slender bright arches during 08:01:30–08:03:30 UT that were clearest in 171 and 193 Å and showed up as bright narrow arcs hovering over FAF-1 in projection to the northeast, but much less prominent than the bright arch after FAF-1.

Figures 14–16 display our standard format results for FAF-2 in four successive *IRIS* samplings. The first sampling (top row of Figure 14, first vertical time marker in Figure 15, no spectra since not of interest) shows the scene seven minutes before FAF-2 brightened: nothing special. The second and third samplings bracket its largest brightness; in the fourth it had diminished (Figure 15). The Hα core showed fibrilar brightening parallel to the filamentary extensions at 1600 Å but not co-spatially.

The blue profiles in Figure 16 are the widest of all our specimens and have deep absorption blends (also from S I and Mn II). They even show central dips in the Si IV lines. In this event the Mg II h & k lines share fully in the Si IV and C II behavior. The similarity between the blue profiles of these six lines is striking, except that the peak ratios reverse from blue-over-red for Mg II h & k and the C II lines to red-over-blue for the Si IV lines.

The central dips of the Si IV lines are not due to optically thick self-absorption because they do not have the same absolute intensity but still share the probability-corrected value. They suggest absorption (scattering) in stationary, likely undisturbed, gas along the line of sight that reaches sufficient opacity for thick self-absorption scattering in the C II and Mg II h & k lines. Outside these cores the six lines exhibit strikingly similar profile shapes.

The blue profiles are not only the brightest but also display the largest raggedness. Inspection of the original spectral images suggests that most of the deeper narrow dips are unidentified blends (for example, the dips just red and blue of the Ni II line between the C II lines). The Mn I and Mn II lines in the h & k wings are also strongly present, in this case with significant blueshifts.

The later samplings (violet and red) show roughly similar profiles at diminishing intensities. The violet sampling shows peak redshift for the Si IV lines and corresponding red-over-blue peak asymmetry for the C II lines, but not for Mg II h & k. The yet later red sampling shows small peak blueshift in the Si IV lines, but similar slight blue-over-red C II and Mg II h & k peak asymmetries and similar line-center redshifts in these doublets (also in the Hα core). The blend blueshifts (also of the Mn I lines) became smaller than in the blue sampling. The Mg II triplet lines appear in absorption in all three samplings. All profiles show some core raggedness.

In summary, FAF-2 showed even wider profiles than FAF-1 but with more symmetry and also with the Mg II h & k wings taking part. The later samplings again suggest a cool-down phase, but with more undisturbed gas along the line of sight because there was no blend-free sampling as the orange profiles of FAF-1 in Figure 13; in contrast, blends including the Mn I lines were present in all three samplings, strongly in the first (blue) and last (red) ones. We speculate that our slanted viewing passed through undisturbed gas at larger height than the FAF samplings because fibrilar canopies tend to rise steeply away from network (containing the reconnecting MCs) to quieter internetwork areas.

4. DISCUSSION

4.1. EB and FAF Properties

EBs and FAFs show interesting similarities and differences. Both phenomena occur in emerging active regions and both probably mark reconnection. EBs do this for reconnection of strong near-vertical fluxtubes in the photosphere and appear as upright flames that remain under the fibrilar chromospheric canopy (see Paper I, Paper II, and further references in Rutten et al. 2013), or even below the upper photosphere when weak (EB-a, b, c). FAFs show distinctive fibrilar morphology and are likely reconnection events along the curved fields that define the canopy.

FAF-1 may have started below the canopy (but was then bright in the Hα core, therefore formally not an EB) but broke through and even became an Hα-core microflare at 08:05 UT, two minutes after it showed its widest ultraviolet profiles (orange in Figure 13).

FAF-2 seemed to reach less high since the blends and line center dips in all samplings in Figure 16 suggest undisturbed cooler stationary gas along the line of sight.

Both EBs and FAFs show outspoken bi-directional jet signatures. For the EBs this is obvious since the *IRIS* spectra of EB-1, the onset of EB-2, and of EB-a, b, and c all show them directly, spatially separated for the first two but mixed up along the line of sight for the other three. The bi-directional nature of the FAFs is more complex because they are less aligned with the line of sight (since also seen in the images as rapid filamentary extensions) and cover larger temperature ranges. The striking difference between the violet sampling of FAF-1 and the blue sampling of FAF-2 in the *IRIS* profiles may simply

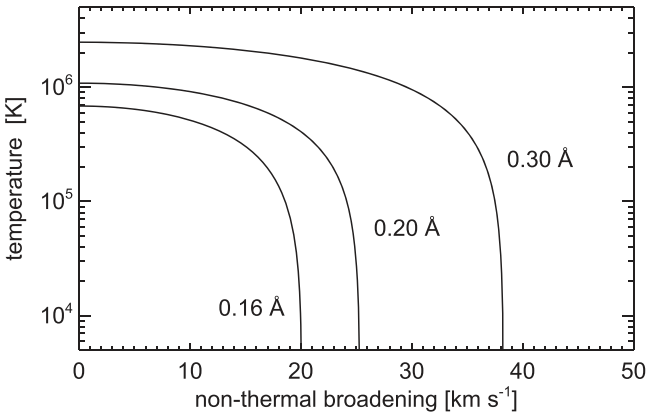

Figure 17. Gaussian profile fitting for Si IV 1403 Å. Each curve shows the combinations of temperature and non-thermal broadening that would produce the specified FWHM values bracketing our observations (0.16 Å for quiet-Sun, the range 0.2–0.3 Å for EBs). The instrumental broadening was set at 4.1 km s^{-1} following De Pontieu et al. (2014) and Tian et al. (2014).

be that the first sampled only one of such jets, the other both. The *IRIS* profiles from B-1 of Peter et al. (2014) then fit in this picture by showing larger Doppler separation.

4.2. EB Temperature Estimation

The first conclusion from observing EBs in the *IRIS* lines is that EBs get very hot, especially in their tops. Such apparent heating to a very high temperature in IBs was the main message of Peter et al. (2014), who wondered whether or not IBs are EBs. Our results show that both EBs and FAFs can produce IB signatures that suggest exceedingly hot events.

How hot precisely? Peter et al. (2014) cited the coronal-equilibrium presence temperature of 80,000 K for Si IV, but remarked that the actual ion distribution may be closer to LTE and peak at lower temperature.

Another way to estimate formation temperature is profile matching. In the idealized case of a convolution of thermal broadening with Gaussian non-thermal broadening and instrumental broadening, the FWHM of the emergent profile from an optically thin homogeneous feature is FWHM $= 1.67\,(\lambda/c)\,\sqrt{2kT/m + \xi^2 + \sigma^2}$, where m is the atomic mass, ξ the non-thermal broadening, and σ the instrumental broadening. Figure 17 shows the possible combinations of thermal and non-thermal broadening that reproduce our observed half-width values. These range so wide that this approach fails without precise knowledge of the non-thermal contribution. In addition, our EBs are either truly thin nor homogeneous.

A better way to establish EB temperatures is profile matching with more sophisticated modeling. Modeling of Hα profiles from EBs has been attempted by Kitai (1983), Berlicki et al. (2010), Bello González et al. (2013), and Berlicki & Heinzel (2014). They all applied ad-hoc perturbations of a static standard model to reproduce observed Hα moustaches. Most defined the perturbation to not extend high, in order to avoid non-observed brightening of the Hα core, but Hong et al. (2014) recognized that the core is actually formed in an overlying fibrilar canopy and should not be modeled as an EB property. They applied a two-cloud fitting model, with one for the EB, the other for the canopy. These fitting exercises all claim that EBs represent temperature enhancements of the low standard model chromosphere by at most a few thousand Kelvin, although usually less. It seems highly unlikely that Si IV lines as displayed here can be obtained from any of them.

In addition to these trial and error fits, numerical EB simulations have been reported by Chen et al. (2001), Isobe et al. (2007), who expanded on the serpentine emergence simulation of Nozawa et al. (1992), Archontis & Hood (2009), and most recently by Nelson et al. (2013b).

The most extensive simulation is the one by Archontis & Hood (2009), who specifically targeted EBs by setting up strong-field U-loop emergence. It also delivered temperature enhancements of the order of 1000 K. However, there was no proper accounting for radiation and no spectral synthesis of, for example, Hα.

The most recent simulation by Nelson et al. (2013b) did not set up an active region emergence event but quiet-Sun magnetoconvection. If their reconnection event was an EB then EBs should appear all over the Sun, contrary to observation. The continuum-brightening, core brightening ("line gap") of Fe I 6303 Å and Hα inner-wing brightening in their synthesized spectra (at top-down viewing, not slanted) suggests that they simulated a pseudo-EB. In any case, the heating was less than 1000 K.

The conclusion must therefore be that the fact that EBs appear in the *IRIS* lines contradicts all EB modeling efforts so far.

4.3. Fine Structure in IRIS Profiles

There is fine-structure raggedness in the green and orange EB-2 profiles in Figure 8, the EB-a, b, and c profiles in Figure 10, the orange and red profiles of FAF-1 in Figure 13, and the FAF-2 profiles in Figure 16.

It can simply be measurement noise, especially at low count values (e.g., in the continua and overlapping wing part of Mg II h & k in Figure 4), but such noise contribution is smaller in bright line cores. The largest counts in the Si IV lines were reached for EB-2 (Figure 8), but also these cores show ragged fine structure.

If the raggedness is not noise then it is either due to blends, which, when present, should re-occur at the same wavelength in different spatio-temporal samplings of a given line, or to profile mapping of fine structure in the event along the line of sight. In the latter case and in optically thick line formation, similar small-scale profile structure should appear at comparable optical depth sampling in different lines per pixel sampling, i.e., slightly further out from the line center in the stronger component of a doublet. In optically thin line formation, a similar profile structure should occur at about the same Dopplershift in different lines per sampling.

Figure 18 details this choice for the two Si IV lines. In all cases their height ratio suggests optically thin or thinish line formation, so that the choice to explain raggedness is between noise, blends, and Doppler mapping of fine structure.

Most larger narrow dips re-occur at the same wavelength in different samplings of the same line (either blue or red) and are therefore blends. The major ones are identified by dashed lines with corresponding line colors. Most of these are blueshifted over about 10 km s^{-1}. There are more blends, especially in the FAF-2 profiles, as noted above.

The EB-a and EB-c profiles in Figure 18 show the largest core raggedness, but also the largest raggedness in the adjacent continua and the largest noise (error bars in Figure 18) because these cores reach only about 200 and 100 counts, respectively

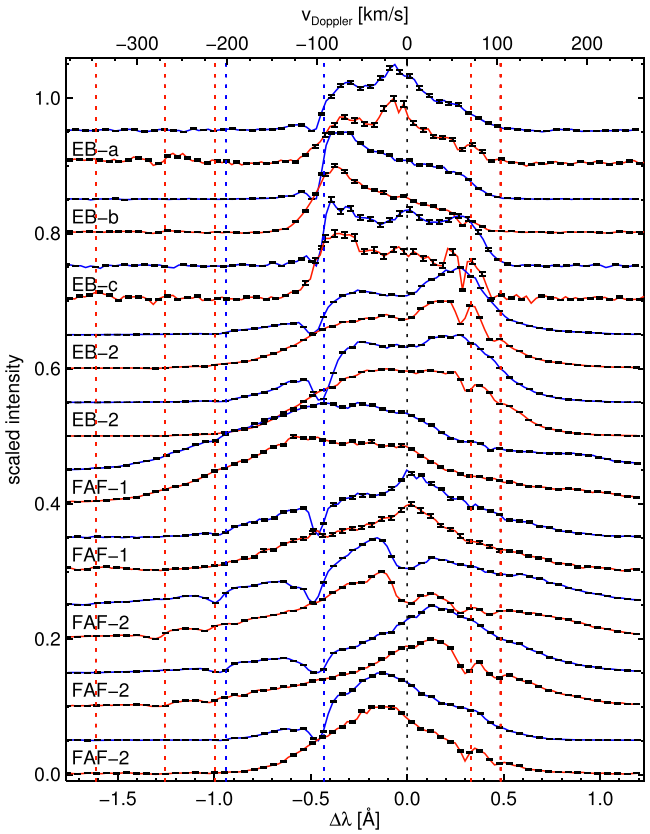

Figure 18. Stagger plot of normalized Si IV profiles to inspect commonality. For each feature that shows profile raggedness (labeled along the left side), selected Si IV 1394 Å profiles are shown in blue with the corresponding Si IV 1403 Å profiles in red, on a common wavelength offset scale with corresponding Dopplershifts along the top. Error bars for Poisson-noise estimates are overplotted in black for every other data point. The intensity range per line is 0.0–0.1, with offsets 0.05. Common dips in profiles of the same color are due to absorbing blend lines. Common dips or humps per blue–red feature pair away from $\Delta\lambda = 0.0$, indicating fine-structure mapping. Other fine structure is mostly measurement noise. The dashed lines, with corresponding color coding, specify the rest wavelengths of major lines, from left to right: O IV 1401.16 Å (red, i.e., blend on Si IV 1403 Å), S I 1401.51 Å (red), Fe II 1401.77 Å (red), Fe II 1392.82 Å (blue, i.e., blend on Si IV 1394 Å), Ni II 1393.32 Å (blue), Si IV 1394 and 1403 Å (black, defining $\Delta\lambda = 0$), Fe II 1403.10 Å (red), Fe II 1403.26 Å (red).

(Figure 10). Indeed, the raggedness appears larger for the weaker red profiles and smaller in the brighter profiles from EB-b.

Finally, the somewhat larger scale deviations from Gaussian profiles in the Si IV cores in Figure 18 often show good similarity between the red and blue pair of profiles per sample. In view of the apparent optically thin (or thinish) line formation of the Si IV lines, we attribute such common fine structure to Dopplershift mapping of features along the line of sight.

For the EBs the presence of Dopplershift fine-structure fits the appearance of EBs in our SST Hα animations as rapidly flickering flames and their bi-directional jet signatures. We surmise that rapid successive, intermittent reconnection of newly arriving opposite-polarity concentrations with varying flux content causes fast variations that eventually end up as fine structure in the resulting hot events.

For the FAFs the wide extent of the profile tails agree with the apparent observed filament extension speeds of 200 km s^{-1}. The picture of thin fast-rising heating events also fits the morphology of the apparent liftoff of thin arcs and resulting bright arches in AIA 304, 171, and 193 Å, in particular after FAF-1.

4.4. Nature of the Hot Events

EB-2 and the two FAFs produced spectra with IB hot-event signatures. EB-1 may have done so too, but its aftermath was not sampled by the *IRIS* slit. The weaker EB-a, b, and c did not. The upshot is that strong EBs can do so. Both FAFs certainly did.

The production of a hot event by upward progressing reconnection is not surprising. When in an EB two photospheric fluxtubes cancel against each other by reconnection, one may expect local temperature increase below a factor two because such fluxtubes tend to obey magnetostatic equipartition with their surroundings. This is indeed seen in the numerical MHD simulation of Archontis & Hood (2009). However, if the reconnection site then proceeds upward, the heating ratio increases because the magnetic energy diminishes less than the gas energy due to larger scale height. A much larger temperature increase may be expected there. In addition, the jet kicks are likely to cause Alfvénic wave generation and dissipation. Therefore, the observational indication that FAF reconnection occurs higher up than EB reconnection may explain why FAFs produce larger IBs and also million-Kelvin arches as FAF-1 did.

Various scenarios come to mind to produce hot gas with spectral blend superimposing by cooler and relatively stationary gas. The first is that this gas is simply undisturbed upper photosphere or chromospheric canopy gas along the line of sight. We suggest that this is the case for the Mn I blends in the Mg II h & k wings for the lines of sight to the feet of EB-1 and EB-2, and may likewise signify small event heights for EB-a, EB-b, and EB-c. Such blends were not present in FAF-1, which had the largest higher atmosphere response of all our events, but for FAF-2 they were prominently present in the blue sampling in Figure 16, superimposed on the widest of all our ultraviolet profiles, and still in the red sampling 17 minutes later. Assuming that these were from undisturbed "normal" gas along the line of sight implies that even FAF-2, which also showed filamentary extensions and AIA hot-diagnostic brightening, did not reach very high in its *IRIS* samplings.

We similarly speculate that the Fe II and Ni II blends on the Si IV and C II lines, which typically show blueshifts up to about 10 km s^{-1}, as also found by Peter et al. (2014), sample adjacent gas harboring upward propagating shocks as those in internetwork regions (e.g., Carlsson & Stein 1997; Leenaarts et al. 2007; Vecchio et al. 2009) and in dynamic fibrils near network and plage (e.g., Hansteen et al. 2006; De Pontieu et al. 2007; Heggland et al. 2007; Langangen et al. 2008).

Alternatively, an EB-like initiation FAF may kick cool photospheric gas up to large height where it can cause line-center dips and absorption blends, or these may originate in a post-bomb cooling cloud. However, such scenarios seem unlikely in view of the lack of large Dopplershifts in the blend lines and central dips.

4.5. EB and FAF Visibility in Mg II 2798 Å

In our *IRIS* spectra the Mg II triplet lines appears with interesting behavior. Their emission profiles closely mimic the C II line shapes in EBs and in the initial EB-like stage of FAF-1, but not in the FAF spectra with stronger IB signatures. Strong

presence of this line suggests a steep, deeply located temperature rise (Pereira et al. 2015). The marked appearances of Mg II 2798 Å in Figures 4, 8 and 10 are indeed in good agreement with the C II and Si IV indications of high temperature already in the lower samplings.

In Figure 13 the line is very strongly present in the first sampling of FAF-1, almost as tall as h & k, so that the startup of FAF-1 resembled a low-atmosphere EB also in this respect. The later Mg II triplet profiles of FAF-1 in Figure 13 are less extraordinary. In all FAF-2 samplings this line appeared in absorption (Figure 16).

4.6. EB and FAF visibility in Hα

Hα is an extraordinary line, as is obvious from any solar Hα filtergram. In EBs and FAFs it is also special. In EB-1 the Hα top producing enhanced C II and Si IV emission is not seen in the first panel of Figure 2, or in the second panel. This suggests that hydrogen was already ionized in the upper part, as one would expect from Si IV visibility. However, in the other rows of Figure 2 and also in Figure 6 the Hα-wing morphology resembles the *IRIS* 1330 Å SJI. We believe that such hot response of Hα stems from severe non-equilibrium recombination of hydrogen (Carlsson & Stein 2002; Leenaarts et al. 2007).

5. CONCLUSIONS

We have combined a comprehensive suite of solar observations. The relatively large field of view, unsurpassed image quality, and fast cadence of the Hα imaging spectroscopy with the SST was indispensable to recognize both EBs and overlying fibrils from their spatial, temporal, and spectral behavior. The full-time full-disk monitoring by *SDO* served to separate EBs and FAFs in AIA 1700 and 1600 Å images and to inspect magnetic field evolution in HMI magnetograms. The *IRIS* SJI, effectively providing high-cadence large-field images in the major *IRIS* lines, are an extremely valuable asset that previous solar ultraviolet spectrometers did not furnish. Last but not least, the spectra in the well-chosen set of *IRIS* lines emerge as varied "unveiled" EB diagnostics not hampered by overlying fibrils and offering rich signatures of what happens in the solar atmosphere at EB and FAF sites. They testify to Pannekoek's dictum that "spectra constitute the astronomer's treasure chest."

We summarize our conclusions for EBs as follows.

1. The cores of Hα and the Mg II h & k lines sample overlying chromospheric fibrils that are unaffected by the underlying EB. In these lines EBs are visible only well away from line center.
2. The *IRIS* Mg II triplet, C II, and Si IV lines sample the Ellerman bomb itself, often with optically thin or near-thin formation of the Si IV cores.
3. These "unveiled" *IRIS* diagnostics indicate that the tops of EBs become much hotter than all previous estimates in the literature.
4. They also give direct evidence of bi-directional jet behavior, with downdrafts of the lower parts and faster updrafts of the hotter upper parts.
5. Subsequently, very hot post-bomb gas appears with wide and complex ultraviolet line profiles that suggest large Dopplershifts, possibly still from bi-directional jets, and much fine-scale structure. Even these remain a sub-canopy phenomenon.

FAFs seem to represent a comparable reconnection phenomenon, but breaking through or progressing along the chromospheric canopy and causing much hotter structures that also become evident in million-Kelvin AIA diagnostics. The main difference with EBs seems that the reconnection is located or proceeds higher, but the blends and line center dips in the *IRIS* profiles from FAF-2 still suggest fairly deep formation.

For future EB modeling, the ultraviolet line profiles from *IRIS* represent highly varied diagnostics furnishing such rich detail that modeling which succeeds in good reproduction is bound to be close to correct. If it does not succeed, then such failure is bound to be instructive also. In this manner, EBs are likely to become the first solar reconnection phenomenon for which detailed modeling may be verified with certainty.

Since FAFs seem of larger interest with regards to upper-atmosphere mass and heat loading, verified EB modeling seems a worthwhile stepping stone to modeling FAFs properly. A good example in this direction is the recent study by Archontis & Hansteen (2014) of the formation of small flares from strong-field magnetoconvection producing serpentine emergence of the type proposed for EBs. Their resulting heating events and coronal jets are more substantial and located higher than EBs, but may describe what we have called FAFs here.

Observationally, the next step is easier: catch EBs and FAFs in joint SST and *IRIS* (and of course *SDO*) observing campaigns targeting emerging active regions well away from disk center with a faster *IRIS* repeat cadence than in data sets 2 and 3. It would also be good to roll *IRIS* to put its slit along the projected vertical per target.

Our research has been partially funded by the Norwegian Research Council and by the European Research Council under the European Union's Seventh Framework Programme (FP7/2007-2013) / ERC grant agreement nr. 291058. B.D.P. was supported by NASA contract NNG09FA40C (*IRIS*). B.D.P., M.C., and L.R.v.d.V. have benefited from discussions at the International Space Science Institute (ISSI) meeting on "Heating of the magnetized chromosphere." *IRIS* is a NASA small explorer mission developed and operated by LMSAL with mission operations executed at NASA Ames Research Center and major contributions to downlink communications funded by the Norwegian Space Center through an ESA PRODEX contract. The SST is operated on the island of La Palma by the Institute for Solar Physics of Stockholm University in the Spanish Observatorio del Roque de los Muchachos of the Instituto de Astrofísica de Canarias. We thank T. Golding, T. Pereira, and H. Skogsrud for assistance with the SST observations and the referee for many useful suggestions.

REFERENCES

Archontis, V., & Hansteen, V. 2014, ApJL, 788, L2
Archontis, V., & Hood, A. W. 2009, A&A, 508, 1469
Bello González, N., Danilovic, S., & Kneer, F. 2013, A&A, 557, A102
Berlicki, A., & Heinzel, P. 2014, A&A, 567, A110
Berlicki, A., Heinzel, P., & Avrett, E. H. 2010, MmSAI, 81, 646
Bernasconi, P. N., Rust, D. M., Georgoulis, M. K., & Labonte, B. J. 2002, SoPh, 209, 119
Carlsson, M., & Stein, R. F. 1997, ApJ, 481, 500
Carlsson, M., & Stein, R. F. 2002, ApJ, 572, 626
Chen, P.-F., Fang, C., & Ding, M.-D. D. 2001, ChJAA, 1, 176

de la Cruz Rodríguez, J. 2010, PhD thesis, Stockholm Univ.
de la Cruz Rodríguez, J., Löfdahl, M. G., Sütterlin, P., Hillberg, T., & Rouppe van der Voort, L. 2015, A&A, 573, A40
De Pontieu, B., Hansteen, V. H., Rouppe van der Voort, L., van Noort, M., & Carlsson, M. 2007, ApJ, 655, 624
De Pontieu, B., Title, A. M., Lemen, J. R., et al. 2014, SoPh, 289, 2733
Ellerman, F. 1917, ApJ, 46, 298
Georgoulis, M. K., Rust, D. M., Bernasconi, P. N., & Schmieder, B. 2002, ApJ, 575, 506
Hansteen, V. H., De Pontieu, B., Rouppe van der Voort, L., van Noort, M., & Carlsson, M. 2006, ApJL, 647, L73
Heggland, L., De Pontieu, B., & Hansteen, V. H. 2007, ApJ, 666, 1277
Henriques, V. M. J. 2012, A&A, 548, A114
Hong, J., Ding, M. D., Li, Y., Fang, C., & Cao, W. 2014, ApJ, 792, 13
Isobe, H., Tripathi, D., & Archontis, V. 2007, ApJL, 657, L53
Kitai, R. 1983, SoPh, 87, 135
Langangen, Ø., Carlsson, M., Rouppe van der Voort, L., Hansteen, V., & De Pontieu, B. 2008, ApJ, 673, 1194
Leenaarts, J., Carlsson, M., Hansteen, V., & Rutten, R. J. 2007, A&A, 473, 625
Leenaarts, J., Pereira, T. M. D., Carlsson, M., Uitenbroek, H., & De Pontieu, B. 2013a, ApJ, 772, 89
Leenaarts, J., Pereira, T. M. D., Carlsson, M., Uitenbroek, H., & De Pontieu, B. 2013b, ApJ, 772, 90
Leenaarts, J., Rutten, R. J., Carlsson, M., & Uitenbroek, H. 2006a, A&A, 452, L15
Leenaarts, J., Rutten, R. J., Sütterlin, P., Carlsson, M., & Uitenbroek, H. 2006b, A&A, 449, 1209
Lemen, J. R., Title, A. M., Akin, D. J., et al. 2012, SoPh, 275, 17
Lites, B. W., Shine, R. A., & Chipman, E. G. 1978, ApJ, 222, 333
Matsumoto, T., Kitai, R., Shibata, K., et al. 2008, PASJ, 60, 95
McMath, R. R., Mohler, O. C., & Dodson, H. W. 1960, PNAS, 46, 165
Nelson, C. J., Doyle, J. G., Erdélyi, R., et al. 2013a, SoPh, 283, 307
Nelson, C. J., Scullion, E. M., Doyle, J. G., Freij, N., & Erdélyi, R. 2015, ApJ, 798, 19
Nelson, C. J., Shelyag, S., Mathioudakis, M., et al. 2013b, ApJ, 779, 125
Nozawa, S., Shibata, K., Matsumoto, R., et al. 1992, ApJS, 78, 267
Pariat, E., Aulanier, G., Schmieder, B., et al. 2004, ApJ, 614, 1099
Pariat, E., Masson, S., & Aulanier, G. 2009, ApJ, 701, 1911
Pereira, T. M. D., Carlsson, M., De Pontieu, B., & Hansteen, V. 2015, ApJ, 806, 14
Pereira, T. M. D., Leenaarts, J., De Pontieu, B., Carlsson, M., & Uitenbroek, H. 2013, ApJ, 778, 143
Peter, H., Tian, H., Curdt, W., et al. 2014, Sci, 346, 1255726
Rutten, R. J. 2003, Radiative Transfer in Stellar Atmospheres, (Lecture Notes) (Utrecht: Utrech Univ.)
Rutten, R. J., Vissers, G. J. M., Rouppe van der Voort, L. H. M., Sütterlin, P., & Vitas, N. 2013, JPhCS, 440, 012007
Scharmer, G. B., Bjelksjo, K., Korhonen, T. K., Lindberg, B., & Petterson, B. 2003, Proc. SPIE, 4853, 341
Scharmer, G. B., Narayan, G., Hillberg, T., et al. 2008, ApJL, 689, L69
Scherrer, P. H., Schou, J., Bush, R. I., et al. 2012, SoPh, 275, 207
Shibata, K., Nakamura, T., Matsumoto, T., et al. 2007, Sci, 318, 1591
Shine, R. A., Title, A. M., Tarbell, T. D., et al. 1994, ApJ, 430, 413
Tian, H., DeLuca, E. E., Cranmer, S. R., et al. 2014, Sci, 346, 1255711
van Noort, M., Rouppe van der Voort, L., & Löfdahl, M. G. 2005, SoPh, 228, 191
Vecchio, A., Cauzzi, G., & Reardon, K. P. 2009, A&A, 494, 269
Vissers, G., & Rouppe van der Voort, L. 2012, ApJ, 750, 22
Vissers, G. J. M., Rouppe van der Voort, L. H. M., & Rutten, R. J. 2013, ApJ, 774, 32 (Paper II)
Watanabe, H., Vissers, G., Kitai, R., Rouppe van der Voort, L., & Rutten, R. J. 2011, ApJ, 736, 71 (Paper I)
Yang, H., Chae, J., Lim, E.-K., et al. 2013, SoPh, 288, 39